Rare earth elements (REEs) in the tropical South Atlantic and quantitative deconvolution of their non-conservative behaviour

Xin-Yuan Zheng [a,1,*], Yves Plancherel [a], Mak A. Saito [b], Peter M. Scott [a,2], Gideon M. Henderson [a]

[a] *Department of Earth Sciences, University of Oxford, South Parks Road, Oxford, OX1 3AN, UK*

[b] *Marine Chemistry and Geochemistry Department, Woods Hole Oceanographic Institution, 266 Woods Hole Road, Woods Hole, MA 02543, USA*

The published version of this manuscript is available at:
http://dx.doi.org/10.1016/j.gca.2016.01.018

[*] Corresponding author.

E-mail address: xzheng75@wisc.edu (X.-Y. Zheng). Tel.: +1 (608) 262-4255.

[1] Now at Department of Geoscience, University of Wisconsin–Madison, WI 53706, USA.

[2] Now at Department of Earth Sciences, University of Cambridge, Downing Street, Cambridge, CB2 3EQ, UK.

Abstract

This study presents new concentration measurements of dissolved REEs (*d*REEs) along a full-depth east-west section across the tropical South Atlantic (~12°S), and uses these data to investigate the oceanic cycling of the REEs. Enrichment of *d*REEs, associated with the redox cycling of Fe-Mn oxides, is observed in the oxygen minimum zone (OMZ) off the African shelf. For deeper-waters, a multi-parameter mixing model was developed to deconvolve the relative importance of physical transport (i.e. water mass mixing) from biogeochemical controls on the *d*REE distribution in the deep Atlantic. This approach enables chemical processes involved in REE cycling, not apparent from the measurements alone, to be distinguished and quantified. Results show that the measured *d*REE concentrations below ~1000 m are dominantly controlled (>75%) by preformed REE concentrations resulting from water mass mixing. This result indicates that the linear correlation between *d*REEs and dissolved Si observed in Atlantic deep waters results from the dominantly conservative behaviour of these tracers, rather than from similar chemical processes influencing both *d*REEs and Si. Minor addition of *d*REEs (~10% of *d*Nd and ~5% of *d*Yb) is observed in the deep (>~4000 m) Brazil Basin, resulting from either remineralization of particles *in-situ* or along the flow path. Greater addition of *d*REEs (up to 25% for *d*Nd and 20% for *d*Yb) is found at ~1500 m and below ~4000 m in the Angola Basin near the African continental margin. Cerium anomalies suggest that different sources are responsible for these *d*REE addition plumes. The 1500 m excess is most likely attributed to *d*REE release from Fe oxides, whereas the 4000 m excess may be due to remineralization of calcite. Higher particulate fluxes and a more sluggish ocean circulation in the Angola Basin may explain why the *d*REE excesses in

this basin are significantly higher than that observed in the Brazil Basin. Hydrothermal venting over the mid-Atlantic ridge acts as a regional net sink for light REEs, but has little influence on the net budget of heavy REEs. The combination of dense REE measurements with water mass deconvolution is shown to provide quantitative assessment of the relative roles of physical and biogeochemical processes in the oceanic cycling of REEs.

1. INTRODUCTION

The rare earth elements (REEs), a sequence of 14 naturally occurring elements with coherent chemical properties, are useful oceanic tracers. In seawater, REE complexation with aqueous ligands, predominantly carbonate ions (e.g., Byrne and Kim, 1990; Wood, 1990), or silicic acid (Akagi et al., 2011; Akagi, 2013), competes with adsorption by marine particles. Because the stability of their aqueous complexes increases with atomic number, the lighter REEs (LREEs) adsorb on particle surfaces relatively more easily (i.e. more particle-reactive) than the heavier REEs (HREEs) (e.g., Byrne and Kim, 1990; Sholkovitz et al., 1994). This dynamic equilibrium between aqueous complexation and particle scavenging fractionates dissolved REEs (*d*REEs) in characteristic ways.

Fractionations between trivalent *d*REEs in seawater are also influenced by other processes, including input from external REE sources and mixing of water masses (Elderfield et al., 1988; Byrne and Sholkovitz, 1996). The behavior of Ce is also mediated by redox transformation between more soluble Ce^{3+} and insoluble Ce^{4+}. Fractionation between the *d*REEs are normally visualized by normalizing measured REE concentrations to a suitable reference, usually shale or another water mass in the ocean (e.g., Zhang and Nozaki, 1998; Nozaki et al., 1999; Alibo and Nozaki, 2004; Zhang et al., 2008; Haley et al., 2014). Such REE patterns can allow for tracing of a variety of oceanic processes (e.g., Sholkovitz et al., 1994; Alibo and Nozaki, 2004; Hatta and Zhang, 2006; Zhang et al., 2008).

Considerable field observations and laboratory experiments have been conducted to

study the marine cycling of REEs (e.g., Elderfield and Greaves, 1982; de Baar et al., 1985; Byrne and Kim, 1990; German et al., 1990; Bertram and Elderfield, 1993; Greaves et al., 1994; Zhang and Nozaki, 1996; Douville et al., 1999; Nozaki and Alibo, 2003; Johannesson et al., 2011; Haley et al., 2014). Other studies have primarily focused on Nd because of the utility of Nd isotopes as a tracer for ocean circulation (e.g., Amakawa et al., 2009; Carter et al., 2012; Grasse et al., 2012; Singh et al., 2012; Grenier et al., 2013; Jeandel et al., 2013; Pearce et al., 2013; Molina-Kescher et al., 2014). In spite of these efforts, substantial uncertainties remain about the processes that control the distribution of REEs in the ocean.

Our ability to unequivocally interpret marine REE patterns and Nd-isotope data is often limited by inability to quantify the influence of physical transport (i.e. water mass mixing) relative to biogeochemical processes (e.g., particle scavenging and remineralization), although both processes are recognized to be important for REEs (e.g., Bertram and Elderfield, 1993; Nozaki and Alibo, 2003; Siddall et al., 2008; Garcia-Solsona et al., 2014; Haley et al., 2014; Molina-Kescher et al., 2014; Hathorne et al., 2015; Stichel et al., 2015). Apparent incompatibility between the nutrient-like profiles of *d*Nd concentrations in the water column and a strong circulation-controlled distribution of seawater Nd isotopic compositions, the so-called "Nd paradox" (Goldstein and Hemming, (2003) and references therein), is a notable example of this limitation.

Another limitation relates to incomplete understanding of exchange processes at the continent–ocean interface. Recent studies, mostly based on Nd, have demonstrated that seawater-sediment interactions on continental margins, a process termed as

120 "boundary exchange" (e.g., Lacan and Jeandel, 2005a; Jeandel et al., 2007), can
121 significantly influence Nd concentration and isotope signature in seawater. Globally,
122 it is thought that boundary exchange could represent the dominant source of the
123 oceanic Nd budget (e.g., Tachikawa et al., 2003; Arsouze et al., 2009; Rempfer et al.,
124 2011). The local expression of this boundary exchange, however, is neither well
125 resolved geographically nor understood mechanically, and existing observations are
126 heterogeneous. Observations suggest that REEs can either be added or removed from
127 the water column near the continent–ocean interface (e.g., Zhang and Nozaki, 1998;
128 Bayon et al., 2011; Carter et al., 2012; Grasse et al., 2012; Grenier et al., 2013;
129 Garcia-Solsona et al., 2014).
130
131 Here we present a new set of concentration data for the 14 *d*REEs collected over full-
132 water-column depths along an east–west zonal section near ~12°S in the tropical
133 South Atlantic. These new measurements significantly augment limited *d*REE (often
134 Nd alone) concentration data available in the South Atlantic (e.g., Jeandel, 1993;
135 German et al., 1995; Rickli et al., 2009; Bayon et al., 2011; Stichel et al., 2012a;
136 Garcia-Solsona et al., 2014), and permit a detailed investigation of processes
137 controlling the *d*REE distribution on a basinal scale. Using a multi-parameter mixing
138 model, we quantified the relative importance of transport and biogeochemical
139 processes in governing the observed *d*REE distribution in the deep tropical South
140 Atlantic for the first time.
141
142 **2. REGIONAL HYDROGRAPHY**
143
144 Seawater samples were collected during the CoFeMUG (KN195–2) cruise aboard the

R/V Knorr (16 November – 13 December 2007) along an E–W transect in the South Atlantic (~12°S) (Fig. 1).

Major water masses sampled in this location can be approximately separated by neutral density (γ^n) surfaces (Fig. 2a), as suggested by Vanicek and Siedler (2002). South Atlantic Central Water (SACW) is found below the mixed layer (~50 m) to ~500 m. Upper-ocean waters (~0–500 m) are transported broadly northwestward or westward via the southern branch of the South Equatorial Current (SSEC), but the eastern side of the section is also influenced by the cyclonic Angola Gyre in the Angola Basin (Fig. 1) (Stramma and England, 1999; Wienders et al., 2000; Mercier et al., 2003). A prominent oxygen minimum zone (OMZ), caused by regional high productivity and low ventilation (Lass and Mohrholz, 2008; Mohrholz et al., 2008), is observed between ~100 m and ~600 m (centred at ~400 m) off the Angolan coast (Fig. 2b).

Antarctic Intermediate Water (AAIW), characterized by a mid-depth salinity minimum immediately below surface waters, extends to ~800 m. Upper Circumpolar Deep Water (UCDW) is observed beneath AAIW. This water mass does not have a clear T–S signature, but can be recognized as a nutrient-rich layer centred at ~1000 m (Fig. 2a). Both AAIW and UCDW spread dominantly northward (Stramma and England, 1999).

North Atlantic Deep Water (NADW), observed below ~1500 m, predominantly spreads southward at the CoFeMUG section, via the major route of the Deep Western Boundary Current and a weaker route near the eastern boundary of the South Atlantic

(Larqué et al., 1997; Stramma and England, 1999; Arhan et al., 2003). Previous studies have suggested that NADW can be further separated into several sub-layers (e.g., Rhein et al., 1995; Stramma and England, 1999; Smethie et al., 2000). The uppermost layer is referred to as upper Labrador Sea Water (ULSW) (e.g., Pickart et al., 1996; Smethie et al., 2000), and is responsible for relatively high temperature and salinity observed at ~1500 m on the western side of the CoFeMUG section (e.g., Rhein et al., 1995; Pickart et al., 1997; Smethie et al., 2000).

Northward-flowing Antarctic Bottom Water (AABW) is found below ~4000 m (γ^n > 28.18) in the Brazil Basin, as indicated by high dissolved Si content (Noble et al., 2012) (Fig. 2a). This water mass is less prominent in the Angola Basin because its northward transport is blocked by the Walvis Ridge to the south (Fig. 1). A small fraction of AABW enters the Angola Basin from the north through deflection at the Romanche Fracture Zone near the equator, but this tongue of AABW gradually loses its identity via mixing with NADW during its transport to the Angola Basin (Warren and Speer, 1991; Larqué et al., 1997; Stramma and England, 1999).

3. SAMPLES AND METHODS

3.1. Sample collection and ancillary data

119 seawater samples from 12 stations were analyzed for *d*REE concentrations. Samples were collected using trace-metal clean techniques; Teflon-coated X–Niskin sampling bottles were deployed on an epoxy-coated CTD rosette attached to a non-metallic line, and were programmed to trip at pre-determined depths. Immediately

following collection, seawater was filtered through 142-mm 0.4-μm polycarbonate plastic sandwich filters in a class–100 laboratory. Filtered samples were acidified to pH of 1.7 with high-purity HCl (Seastar). All bottles, tubing and filters were acid-cleaned before use.

Salinity (S), potential temperature (T) and dissolved oxygen (dO_2) were measured *in-situ* with CTD-mounted sensors. CTD data were not available at several water-depths (mostly ≥1000 m) at Station 1, 7, 9 and 18 due to sensor malfunction. For these depths, T and S data were interpolated from the World Ocean Atlas 2009 (WOA09) seasonal (October–December) climatology (Table A.1). The interpolated T and S values are in good agreement with shipboard measurements where both are available. Nutrients (e.g., dissolved silica and phosphate), *d*Fe, and *d*Mn concentrations were also measured across the CoFeMUG section (Noble et al., 2012; Saito et al., 2013). Data are available from http://bcodmo.org, and also in the GEOTRACES Intermediate Data Product (Mawji et al., 2015).

3.2. Analytical procedure for *d*REE concentrations

Dissolved REE concentrations were measured at the Department of Earth Sciences, University of Oxford, following Zheng et al. (2015). Briefly, ~100 ml of filtered seawater was spiked with ^{142}Ce–^{145}Nd–^{171}Yb. REEs were preconcentrated with Fe co-precipitation, followed by purification through a simple one-stage ion-exchange chromatographic separation using AG 1–X8 anion exchange resin (100–200 mesh, Bio-Rad) to remove Fe. Dissolved REEs were analyzed on a magnetic sector-field ICP–MS (Element 2, Thermo Scientific) coupled with a desolvating nebulizer system

(Aridus 1, CETAC). Oxide interferences (i.e. Ba oxides on Eu, and LREE oxides on HREEs) were negligible (<~1%). The procedural blank, typically <1% for all REEs except for Ce (~8%), was monitored for each batch of sample pre-treatment, and corrected batch by batch. Repeated measurements of an in-house seawater standard throughout the course of this study yielded an external reproducibility of <3% (1σ, n=19) for all REEs. Measurements performed on GEOTRACES intercalibration samples (BATS) agree with results reported by other laboratories within 10% (van de Flierdt et al., 2012; Zheng et al., 2015).

3.3. Ce anomaly calculation

The extent of oxidative removal of Ce, due to formation of insoluble Ce^{4+}, can be quantified by the "Ce anomaly", which represents the ratio between the measured *d*Ce concentration and the predicted Ce concentration (Ce*) that would occur without this oxidative removal process (i.e., the Ce concentration obtained by interpolating between its neighbouring REE elements). The Ce anomaly in this study is defined as $Ce/Ce^* = [(2 \times Ce_{SN} / (La_{SN} + Pr_{SN})]$, where REE_{SN} indicates REE concentrations normalized to the post-Archean Australian shale (PAAS; McLennan, 1989). Positive, or negative, Ce anomalies indicate that Ce/Ce* values are greater, or smaller, than 1.

3.4. Multi-parameter mixing model

3.4.1. Model description

The oceanic distribution of *d*REEs is controlled by mixing of different water masses,

and by non-conservative processes, such as particle scavenging, remineralization and boundary exchange (e.g., Bertram and Elderfield, 1993; Nozaki and Alibo, 2003; Siddall et al., 2008; Singh et al., 2012; Haley et al., 2014). An inverse model, based on optimum multiparameter (OMP) analysis, was developed to deconvolve the effect of conservative mixing and non-conservative processes from the observed concentrations (e.g., Tomczak and Large, 1989; Karstensen and Tomczak, 1998; Hupe and Karstensen, 2000; Singh et al., 2012).

Briefly, the observed concentration (x_{obs}^{j}) of a conservative tracer *j* in a given water parcel can be expressed as a mixture of *n* pre-defined end-member water types as:

$$\sum_{i=1}^{n} f_i \times x_i^j = x_{obs}^j \quad \text{(Eq. 1)}$$

where f_i represents the fraction of end-member water type *i*, and x_i^j represents the characteristic value of the tracer *j* in the pre-defined end-member water type *i*.

For non-conservative tracers, a residual term (Δx^j) is added to capture the net effect of all non-conservative processes:

$$\sum_{i=1}^{n} f_i \times x_i^j + \Delta x^j = x_{obs}^j \quad \text{(Eq. 2)}$$

Mass conservation requires that the mass fractions (f_i) sum to 1:

$$\sum_{i=1}^{n} f_i = 1 \quad \text{(Eq. 3)}$$

The number and type of available tracers sets the total number of equations. After

defining the end-member properties characteristic of each tracer (x_i^j), the system of conservation equations can be solved for the mixing fractions (f_i), and the non-conservative terms (Δx^j) simultaneously.

In this study, potential temperature and salinity were used as conservative tracers, and dissolved silicate (Si), phosphate (PO_4), *d*Nd and *d*Yb were used as non-conservative tracers. Nd and Yb were selected to represent the LREEs and HREEs respectively.

The analysis was limited to samples below water depths of ~1000 m at the CoFeMUG section to avoid complications associated with defining end-members in the shallow ocean, where local variability can be important, and where the concept of water mass mixing is less applicable. Four end-members were defined: UCDW, upper NADW (UNADW), lower NADW (LNADW) and AABW. UNADW corresponds to ULSW and classic Labrador Sea Water, and LNADW refers to the rest of NADW fed by overflows at the Greenland–Iceland–Scotland ridge (e.g., Marsh, 2000; Vanicek and Siedler, 2002).

The system described above consists of 7 equations (i.e. based on T, S, Si, PO_4, *d*Nd, *d*Yb and mass conservation). A fixed $\Delta Si/\Delta PO_4$ ratio of 40 was used in the model to reduce one unknown (i.e., ΔSi), based on previously observed and modelled results (e.g., Takeda, 1998; Hupe and Karstensen, 2000). This system is just-determined (i.e., the number of unknowns equates to the number of equations) for 4 end-member mixing; the 7 unknowns are the mass fractions of each of the 4 end-member water masses (f_1 to f_4), and the non-conservative terms ΔPO_4, ΔNd and ΔYb.

This system of equations was solved using the conjugate gradient method, which is a widely used iterative method for solving systems of linear equations (Tarantola, 2005). Computation using this method is inexpensive and fast for each iterative step, although sometimes it may require long iterations. The conjugate gradient method used in our model contrasts with the non-negative least-squares regression method used commonly in the extended OMP analysis, which forces solution to be non-negative for the non-conservative terms (e.g., Hupe and Karstensen, 2000). This change was necessary because the terms ΔNd and ΔYb can be either negative (i.e. removal) or positive (i.e. addition).

3.4.2. Definition of end-member characteristics

End-member properties (Table 1) for the 4 water masses (UCDW, UNADW, LNADW and AABW) were pre-defined based on observational data in the corresponding neutral-density layers (Vanicek and Siedler, 2002). End-member values for T, S, Si, PO_4 were selected using historical data from the World Ocean Circulation Experiment (WOCE, http://www.ewoce.org). For northerly-sourced waters, end-member values were based on data measured at $27.75 < \gamma^n < 27.89$ (~1000–2000 m) between 30°N and 60°N in the North Atlantic for UNADW, and at $27.89 < \gamma^n < 28.12$ (~2000–5000 m) in the same area for LNADW. For southerly-sourced waters, end-member values were taken from data collected in areas south of 15°S at $27.55 < \gamma^n < 27.75$ (~500–2000 m) for UCDW, and at $\gamma^n > 28.12$ (>~4000 m) between 35°S and 45°S for AABW. Because of the limited availability of *d*Nd and *d*Yb concentration data relative to that of traditional hydrographic tracers, large geographic areas were chosen to cover reasonable amount of *d*Nd and *d*Yb data, so that end-member values for all tracers of

each water mass can be defined in the same geographic area. The hydrographic end-member values defined in this study are consistent with those defined for these water masses in previous studies (Larqué et al., 1997; Lee et al., 2003).

End-member values for *d*Nd and *d*Yb concentrations were based on the available data in the same regions used to define other tracers, and are given in Table 1. The larger areas used provide ~15–30 observations for *d*Nd and ~8–20 for *d*Yb for each end-member. Characteristic *d*Nd and *d*Yb concentrations for UNADW and LNADW were defined based on *d*REE data reported by Elderfield and Greaves (1982), de Baar et al. (1983, 1985), Piepgras and Wasserburg (1983, 1987), Sholkovitz and Schneider (1991), Sholkovitz et al. (1994), Lacan and Jeandel (2004, 2005b), Rickli et al. (2009) and Stichel et al. (2015). The pre-defined *d*Nd end-member values for the two water masses in this study agree well with the latest measurements from the GEOTRACES GA02 section (Lambelet et al., 2016).

For UCDW and AABW, end-member values were based on *d*REE data reported in Jeandel (1993), German et al. (1995), Rickli et al. (2010), Stichel et al. (2012a), Garcia-Solsona et al. (2014), Hathorne et al. (2015) and our *d*REE data (>100 new measurements) from GEOTRACES GA10 section along ~40°S (http://www.egeotraces.org). Although *d*Nd and *d*Yb end-member values for UCDW were based on a broadly defined geographic area (i.e., south of 15°S), they show little difference if a geographic constraint consistent with AABW (i.e., 35–45°S) was applied, because the majority of existing *d*Nd and *d*Yb data for UCDW were measured around ~40°S. A major change in *d*Nd concentrations in AABW was observed between the area around ~40°S (>30 pmol/kg Nd) and Polar regions south

of ~50°S (~25 pmol/kg *d*Nd) (Stichel et al., 2012a; German et al., 1995; Garcia-Solsona et al., 2014; Hathorne et al., 2015), indicating significant addition of *d*Nd within these areas. The detailed mechanism for this addition, however, is not clear. In this study, we defined *d*Nd and *d*Yb end-member values based on data close to ~40°S, so that our deconvolution results do not integrate any *d*REE addition occurring south of ~40°S.

3.4.3. Perturbation experiments and robustness evaluation

The sensitivity of the deconvolution results to the selection of end-member values was assessed by numerical Monte Carlo perturbation experiments. Uniformly distributed random noise was imposed on the pre-defined end-member values to account for the natural variability in regions where the end-members were defined (Table 1), and was also added on the measured data to reflect the uncertainty associated with the analytical precision of the measurements (Fig. S1). A uniform distribution of noise was used, rather than a normal distribution, so that the results of perturbation experiments were not biased towards the mean end-member values provided in Table 1. Any combination of end-member values within the range of ± 1 standard deviation provided in Table 1 had equal chance of being tested in our model. A total of 250,000 perturbation experiments were conducted for each sample in the section to fully characterize the probability distributions of the solutions.

The robustness of the spatial pattern of ΔNd and ΔYb values is assessed using a rank analysis technique. The ΔNd or ΔYb values for all the samples along the CoFeMUG section are first ranked, independently, for each Monte Carlo perturbation experiment.

The number of times that the ΔNd or ΔYb values of each sample rank in the bottom or top third, relative to other samples in the section, is then counted across all Monte Carlo experiments. This count provides a measure of the probability that a given sample produces ΔNd or ΔYb results low or high relative to other samples in the section across all perturbation experiments. To assess whether the resulting count is due to chance alone, it is compared with the number of counts expected from a random process. The probability that a particular ΔNd or ΔYb value ranks in the bottom or top third by chance alone is 1/3. For 250,000 Monte Carlo experiments, the binomial distribution predicts, with a 95% confidence level, that the number of times a random number will fall in the bottom or top third is 83,333 ± 388 (Borradaile, 2003). Samples with a count falling outside this range are therefore considered to have ΔNd (or ΔYb) values that are robustly low or high.

4. RESULTS

4.1. Dissolved REE concentrations

For simplicity, only the distributions of *d*Nd, *d*Yb, *d*Ce and Ce anomaly are shown in Fig. 3. Neodymium represents the *d*LREEs (La to Dy), and Yb represents *d*HREEs (Ho to Lu). Cerium is shown because of its unique redox properties. Dissolved concentrations for all 14 REEs are reported in Appendix (Table A.1). Representative vertical profiles are available in Supplemental Material (Fig. S2).

Characteristic *d*Nd profiles along the CoFeMUG section show a decrease from ~17 pmol/kg in the surface to ~13 pmol/kg at ~400–1000 m, followed by a continuous

increase towards the bottom. Notable exceptions are observed at stations affected by the OMZ off the Angola shelf (Stations 13–17), where secondary *d*Nd maxima develop at ~400 m, coincident with the core of the OMZ (Fig. 3). Typical *d*Yb profiles show a ~2-fold increase from ~2.5 pmol/kg in surface waters to ~5.5 pmol/kg at ~1000–1500 m, followed by a <~25% increase towards the bottom. The *d*Ce concentrations display surface maxima at all stations, followed by a rapid decrease with depth. They remain low below ~400 m. Secondary *d*Ce maxima are found at ~400 m at stations 15 and 17 within the OMZ.

The *d*REE distributions show clear lateral variability across the section (Fig. 3). Surface water *d*REE concentrations are high close to the Angola coast, and decrease offshore from Station 18 to Station 17 before reaching relatively constant values at the remaining open-ocean stations. Plumes of high *d*Nd, *d*Ce and Ce anomaly values are observed, coincident with the subsurface OMZ at ~400 m off the Angola shelf (Fig. 3). Similar elevated *d*Nd concentrations have previously been observed in the nearshore OMZ in the eastern North Atlantic (~20°N) (Stichel et al., 2015). A small east-to-west *d*Yb decrease gradient exists at ~400 m at the CoFeMUG section, although the *d*Yb plume is not well defined. Below ~4000 m, deep waters in the Brazil Basin show higher *d*Nd and *d*Yb concentrations than in the Angola Basin.

Three notable features characteristic of the *d*Ce distribution along the CoFeMUG section include the low concentrations above the mid-Atlantic ridge (MAR) (Fig. 3), a small plume of high *d*Ce in the OMZ at ~400 m off the Angola coast, and a prominent plume of *d*Ce near the African continental margin between ~1000 m and ~4000 m (Fig. 3).

Shale-normalized REE patterns from representative stations in the Brazil Basin (Station 4) and the Angola Basin (Station 15) are shown in Fig. 4. REE patterns are relatively flat in surface waters, showing only weak Ce negative anomalies. These features are commonly observed in other parts of the ocean (e.g., Bertram and Elderfield, 1993; Stichel et al., 2012b; Jeandel et al., 2013; Garcia-Solsona et al., 2014), and likely reflect the influence of terrigenous input. The degree of HREE enrichment and the negative Ce anomalies generally become stronger with increasing depth, as observed previously for the South Atlantic (German et al., 1995; Garcia-Solsona et al., 2014).

4.2. Deconvolution results of the end-member mixing model

4.2.1. Mixing fractions

The mixing fractions for UCDW, NADW (combined UNADW and LNADW) and AABW are shown in Fig. 5. The results are consistent with previous modelling results and the hydrographic observations for the South Atlantic (e.g., Larqué et al., 1997; Stramma and England, 1999).

The fraction of UCDW is maximum (~100%) at ~1000 m, and gradually decreases to <20% at ~2000 m. The diminished UCDW fraction with depth is balanced by the increased influence of NADW, which dominates the section between ~2000 m and ~3500 m with fractions reaching >80%. Below ~3500 m, the fraction of NADW progressively declines to <20% near the seafloor in the Brazil Basin, while AABW

fraction increases from <20% to >80%. Consistent with hydrographic observations, the fraction of NADW remains high (~80%) in the deep Angola Basin, where the fraction of AABW is low (i.e. ~20%).

4.2.2. Non-conservative components: ΔNd and ΔYb

The non-conservative components ΔNd and ΔYb represent the difference between measured *d*Nd and *d*Yb concentrations and the concentrations expected only by mixing of the pre-defined end-member water masses. The patterns of ΔNd and ΔYb for all samples deeper than 1000 m across the CoFeMUG section are shown in Fig. 6. Negative values indicate net removal; positive values imply net excess. The relative contributions of ΔNd and ΔYb to the total measured *d*Nd and *d*Yb concentrations are shown in Fig. 7. Results of the mixing model (Fig. 6 and 7) draw out features that are related to geochemical processes affecting the REEs, but are not visible from the distribution of total concentrations alone (Fig. 3).

The strongest *d*Nd removal (ΔNd < -1 pmol/kg) is observed above the Mid-Atlantic Ridge (MAR) (Fig. 6), representing >5% of the measured *d*Nd concentrations (Fig. 7). High Nd removal (ΔNd ≈ ~-1 pmol/kg) was also found at depth between ~1000 m and 3000 m in the Brazil Basin (e.g., Station 1), representing ~5% of the total *d*Nd concentrations for these samples. Addition of *d*Nd, up to 5pmol/kg, was observed in the deep Brazil Basin (>~3500 m). Two plumes of significant *d*Nd excess were found in the Angola Basin at depths of ~1500 m and below ~4000 m respectively, with ΔNd values generally increasing towards the Angola margin. The *d*Nd excess at ~4000 m, with ΔNd values of up to ~8 pmol/kg, accounts for up to ~25% of the total *d*Nd

concentrations, and is the strongest non-conservative signal along the section. In comparison, the excess *d*Nd plume at ~1500 m, with ΔNd values of ~4 pmol/kg, accounts for ~20% of the measured total *d*Nd concentrations.

In contrast to *d*Nd, no net removal of *d*Yb was found above the MAR, and, in most areas of the Brazil Basin, *d*Yb shows minor excess of <0.5 pmol/kg, representing only <5% of the measured *d*Yb. Excess *d*Yb values of up to ~1.25 pmol/kg, which accounts for as much as ~20% of the total *d*Yb concentrations, were observed in the Angola Basin. Unlike *d*Nd, *d*Yb shows almost ubiquitous excess throughout that basin. Although two plumes are suggested in the contour plots at ~1500 m and ~4000 m (Fig. 6 and 7), they are not as well-separated as those for *d*Nd.

4.2.4. Robustness of spatial patterns of the ΔNd and ΔYb results

The spatial patterns of *ΔNd and ΔYb* across the CoFeMUG section are robust, as revealed by the rank analysis on all results of Monte Carlo perturbation experiments (Fig. 8). The modelling results are not governed by chance, because ΔNd and ΔYb results that rank in the bottom or top third fall outside the counts predicted by the binomial distribution for a random process (i.e. 83,333 ± 388, 95% confidence level) for all samples.

The spatial distribution of probability shown in Figure 8 is based on the number of times that ΔNd (and ΔYb) results of a sample are higher or lower than the results of two thirds of samples in the section across all perturbation experiments. This treatment captures the inherent relationship of a ΔNd or ΔYb result, regardless of its

actual value, relative to all other samples in the CoFeMUG section across 250,000 perturbation experiments, and directly characterizes the likelihood of each ΔNd and ΔYb result being high (or low) across the section. The probability that ΔNd results rank in the bottom-third is highest (>0.9) in areas above the MAR and >0.7 between ~1000-3000 m at Station 1 (Fig. 8c). The probability that ΔNd results fall in the top-third is high in the deep Brazil Basin (~0.7), and is the highest (>~0.7-0.9) at ~1500 m and below ~4000 m near the continental margin in the Angola Basin (Fig. 8a). Although the fraction of non-conservative behaviour for *d*Nd is high (up to ~15% of total *d*Nd) at ~1000 m in the west side of the section (Fig. 7), the probability that ΔNd results fall in the top-third in this area is ~0.4 (Fig. 8a), close to that predicted for a random process (~0.33), indicating that the results in this region are sensitive to the choice of end-member values. Except for this region, the probability distributions of ΔNd (Fig. 8a, c) are consistent with key features of the absolute and relative ΔNd patterns (Fig. 6 and 7), indicating that the ΔNd patterns are statistically stable. That is, patterns in Fig. 6 and 7 are relatively insensitive to the selected end-member values. Similarly, good agreement was observed between the probability distributions of ΔYb (Fig. 8b, d) and ΔYb patterns (Fig. 6 and 7), suggesting that ΔYb patterns are also robust.

5. DISCUSSION

5.1. Release of REEs from water-column reduction of oxides

High *d*REE concentrations in surface waters near the Angola coast (Station 17 and 18) are observed (Fig. 3), and agree with high *d*Nd concentrations observed previously in

this region (Rickli et al., 2010). Based on Nd-isotope evidence, the high *d*Nd concentration was attributed to local decomposition of Fe-Mn oxides in the water column, or in shelf sediments, under low oxygen conditions (Rickli et al., 2010). This interpretation is consistent with more recent *d*Fe and *d*Mn observations, which are also high in coastal surface waters (Noble et al., 2012).

Dissolved REE enrichment is also observed in the OMZ (Fig. 3). This enrichment is similar, albeit of smaller magnitude, to the enrichment observed at the oxic/anoxic interface in the water column in anoxic basins. It has been shown to be caused by the desorption of REEs upon reductive dissolution of Fe-Mn oxides (e.g., de Baar et al., 1988; German and Elderfield, 1989; German et al., 1991a; Sholkovitz et al., 1992; Schijf et al., 1995). The close association between *d*REEs and the redox cycling of Fe and Mn in the OMZ along the CoFeMUG section is demonstrated by the significant positive correlation between *d*REEs (including the Ce anomaly) and *d*Fe, or *d*Mn, observed for the data at stations in the OMZ (dO_2 < ~60 μM) at ~400 m (a quasi-isopycnic layer with density of ~27.0-27.1) (Fig. 9). No such correlation is visible in data from the same depth from stations located outside the OMZ.

The close association between REEs, Fe and Mn in the OMZ is also reflected in the REE patterns (Fig. 10). Seawater *d*REE concentrations at ~400 m were normalized to the mean *d*REE concentrations averaged across all CoFeMUG samples at ~1000 m to better reveal small variations in *d*REE patterns. Compared to seawater outside the OMZ (Station 1–9), seawater influenced by the OMZ shows REE patterns characterized by pronounced *d*LREE enrichment and weak negative or positive Ce anomalies (Fig. 10a). These features are consistent with reduction of Fe-Mn oxides

because these particles display typical LREE-enriched patterns with prominent Ce excess (e.g., de Baar et al., 1988; German and Elderfield, 1989; Sholkovitz et al., 1994; Bayon et al., 2004; Freslon et al., 2014) (Fig. 10b).

The seawater REE patterns provide evidence for *in-situ* release of *d*REEs from reduction of Fe-Mn oxides in the water-column of the OMZ. Lateral transport of *d*REEs released from sediments on the African shelf may also occur, but if lateral transport were the dominant REE source, one would have expected a progressive depletion of *d*LREEs relative to *d*HREEs with increasing distance from shore due to continuous scavenging, and progressive development of a negative Ce anomaly towards that of seawater outside the OMZ. More pronounced *d*LREE enrichment and positive Ce anomalies observed at Station 15 and 17 relative to the REE pattern found at Station 18, however, clearly contradicts the expected trend, suggesting *in-situ* regeneration of *d*REEs (Fig. 10a). This observation is consistent with that in the eastern North Atlantic (~20°N), where Nd isotopes also indicate major release of scavenged Nd from particles in the OMZ off the Mauritanian shelf (Stichel et al., 2015). Our data indicate a local dO_2 threshold of ~25 μM (i.e., observed at Station 17 and 15) that enables reductive release of *d*REEs from Fe-Mn oxides. This value is slightly higher than that reported for the OMZ in the northwest Indian Ocean (dO_2 < ~15 μM) where recycling of *d*REEs from particles occurs (German and Elderfield, 1990), but the observation in the OMZ in the eastern North Atlantic demonstrates that desorption of *d*REEs from particles can happen at even higher dO_2 concentrations (~40 μM) (Stichel et al., 2015).

In contrast, secondary concentration maxima are absent in *d*Nd profiles at water

depths corresponding to the OMZs in the eastern equatorial Pacific, southeast Pacific and Arabian Sea where local dO_2 concentrations can be <15 μM (Grasse et al., 2012; Jeandel et al., 2013; Goswami et al., 2014). It remains unclear whether these previous observations truly reflect a lack of *d*Nd enrichment in OMZs due to the relatively low spatial and depth resolution of available data. Enrichment or depletion of an element may only become apparent when individual profiles are considered in the context of its distribution at the basinal scale, as demonstrated by *d*Yb from the CoFeMUG section, whose enrichment in the OMZ is not visible from any individual profile (Supplemental Material, Fig. S2), but is clearly suggested by an east–west concentration gradient at ~400 m across the section (Fig. 3). Alternatively, the contrasting observations indicate that, besides dO_2 contents, multiple parameters, including regional REE input, particle dynamics and hydrographic conditions collectively determine the REE cycling in OMZs.

5.2. The dominance of preformed *d*REEs in Atlantic deep waters

Concentrations of *d*REEs in deep-waters of the central Atlantic are dominantly controlled by mixing of the major Atlantic water masses (>75%), rather than by geochemical processes operating during transit of these waters from their source regions (Fig. 7). Deviations from purely conservative mixing for the *d*REEs are up to a maximum of 25%. The dominance of the preformed component in setting deep-water *d*REE concentrations explains why these concentrations resemble the general water mass structure of the South Atlantic (Fig. 2 and 3). For example, higher *d*REE concentrations in the deep Brazil Basin than those observed in the deep Angola Basin is largely related to the presence of AABW in the Brazil Basin.

589

590 Preformed *d*REEs are particularly important in setting observed *d*REE concentrations
591 in the deep Brazil Basin (Fig. 7), where ~95% of the observed *d*Yb, and ~90% of *d*Nd,
592 can be explained by conservative water-mass mixing. A slightly higher percentage of
593 preformed *d*Yb than that of preformed *d*Nd is consistent with the general behaviour of
594 REEs in the ocean that HREEs are less particle-reactive than LREEs (e.g., Wood,
595 1990; Sholkovitz et al., 1994).

596

597 The large preformed contribution to deep-waters in the Brazil Basin predicts that
598 *d*REEs should correlate well with other conservative tracers, such as *d*Si, which
599 behaves almost conservatively in the deep South Atlantic (e.g., Broecker et al., 1991;
600 Sarmiento et al., 2007). This explains the particularly good linear correlation between
601 *d*REE and *d*Si ($R^2 > 0.9$) observed below ~2000 m in the Brazil Basin (Fig. 11). The
602 larger non-conservative behaviour of *d*REE concentrations in the deep Angola Basin
603 may explain the poorer *d*REE–*d*Si relationship observed there (Fig. 11).

604

605 Our results indicate that the linear *d*REE–*d*Si relationship in the deep tropical Atlantic
606 results mostly from water mass mixing due to dominantly conservative behaviour of
607 these elements, rather than from local biogeochemical processes coupling the two
608 elements. This conclusion contrasts with studies that have suggested a direct link
609 between the cycling of *d*Nd and *d*Si in the high-latitude Southern Ocean based on the
610 observed linear relationships between the two elements (e.g., Stichel et al., 2012a;
611 Garcia-Solsona et al., 2014; Hathorne et al., 2015). A possible explanation that
612 reconciles our results with these previous studies relies on the large contrast in opal
613 fluxes between our study region and the Southern Ocean. High opal fluxes in the

Southern Ocean may facilitate strong local regeneration of *d*REEs from dissolution of biogenic silica in deep waters in this specific region. In addition, this *d*REE regeneration could be further promoted by strong vertical mixing in certain areas of the Southern Ocean. After deep-water *d*REEs and *d*Si are exported from the Southern Ocean into the sub-tropical and tropical South Atlantic where opal flux is low, their distributions are no longer controlled by a coupled REE and opal cycle, but essentially governed by water mass mixing. A coupled REE–Si cycle was proposed to explain general concentration profiles of *d*REEs in the ocean (Akagi, 2013), our results, however, demonstrate that such a coupling is not necessarily true on a global scale.

5.3. Suggested REE sources from sedimentary Fe oxides and remineralization of calcite

The deconvolution enables boundary addition of *d*REEs, previously observed for *d*Nd in other locations (e.g., Singh et al., 2012; Garcia-Solsona et al., 2014), to be quantified for waters of the tropical south Atlantic. Our deconvolution results show regions where up to 25% of the measured *d*REE concentrations cannot be explained by mixing of water-mass end-members, and, by contrasting the spatial pattern of the addition, provide clues about possible mechanisms of boundary addition.

Addition of *d*REEs (~10% for *d*Nd and ~5% for *d*Yb) is observed in AABW in the deep Brazil Basin (>~4000 m), and can be explained by release of *d*REEs from *in-situ* remineralization of particles, or by accumulation of remineralized *d*REEs along the flow path of AABW from ~40°S. More significant REE addition (up to ~25%) is seen

on the eastern side of the section, in the Angola Basin, with Nd excess seen at two depths (~1500 m and below ~4000 m), and Yb excess at all depths below ~1500 m (Fig. 6 and 7). The different distribution of ΔNd and ΔYb in the Angola Basin may result from different particle reactivity between LREEs and HREEs. Because HREEs are less particle-reactive than LREEs in seawater (e.g., Wood, 1990; Sholkovitz et al., 1994), signals of Yb addition are expected to survive longer in the water column, so that they can be mixed or advected from their source. In contrast, Nd is more quickly scavenged by particles, so that signs of its addition are likely to be more restricted spatially.

In contrast to the increased *d*REE concentrations seen at ~400 m in the OMZ, it is unlikely that remineralization of particulates in the water-column can explain the excess REE concentrations seen at ~1500 m in the Angola Basin. The water is well-oxygenated below ~1000 m (>100 μmol/kg), so that reduction of Fe-Mn oxides in the water column can be ruled out. Because the strongest *d*REE excesses are seen close to the margin (Fig. 6 and 7), release of *d*REEs from slope sediments seems the most plausible source to explain the 1500 m REE excess. These *d*REE excesses are accompanied by high *d*Fe concentrations (Noble et al., 2012), suggesting that the release of *d*REEs from sediments may involve reduction of Fe oxides in the sediment. Iron oxides are characterized by positive Ce anomalies (e.g., de Baar et al., 1988; German and Elderfield, 1989; Sholkovitz et al., 1994; Bayon et al., 2004; Freslon et al., 2014), so their decomposition may also explain the less pronounced negative Ce anomaly (i.e., higher Ce/Ce^{*} values) observed at this depth (Fig. 3).

There is no noticeable development of less pronounced negative Ce anomaly

associated with the REE excess below ~4000 m (Fig. 3), suggesting that a different processes must be responsible for this deep REE excess. This 4000 m *d*REE excess occurs just below the calcite saturation depth (CCD) (Feely et al., 2004), suggesting that dissolution of calcite might release REEs scavenged from shallower depths back to seawater. Carbonates commonly show seawater-like negative Ce anomalies (Palmer, 1985; Haley et al., 2005; Akagi et al., 2011), rather than positive Ce anomalies typically associated with Fe-Mn oxides and organic matters (Bayon et al., 2004; Freslon et al., 2014), so that dissolution of calcite might explain the absence of a Ce anomaly associated with the increased trivalent REEs below ~4000 m.

The excess *d*REEs in the Angola Basin is significantly higher than that found in the Brazil Basin, especially given the fact that AABW is almost absent from the deep Angola Basin (Fig. 5). One explanation for this asymmetry is that particulate fluxes near the African coast are higher, sustained by high surface productivity (Henson et al., 2012), and that seawater *d*REE concentrations in the upper ocean (<1000 m) in the Angola Basin are also elevated. Together, these two conditions produce a stronger "REE pump", leading to higher downward REE fluxes in the deep Angola Basin relative to the Brazil Basin.

In addition, ΔNd and ΔYb results also contain a component of a path-integrated sum of all non-conservative processes along the flow path from the regions where end-member values were defined. Compared to more vigorous transport of NADW along the Deep Western Boundary Current and inflow of AABW, the higher percentage of non-preformed *d*REEs in the Angola Basin may be caused by older water mass ages and a more sluggish circulation in this basin, which allow for accumulation of more

689 regenerated *d*REEs as compared to the Brazil Basin.

690

691 **5.4. Scavenging of *d*LREEs above the mid-Atlantic ridge (MAR)**

692

693 Recent results have clearly indicated that mid-ocean ridges can represent significant
694 sources of dissolved trace metals, such as Fe, to the water, and metals released from
695 hydrothermal vents can transport over hundreds to thousands of kilometers away from
696 the source (e.g., Klunder et al., 2012; Nishioka et al., 2013; Saito et al., 2013;
697 Fitzsimmons et al., 2014; Hatta et al., 2015; Resing et al., 2015). Such addition has
698 also been seen for *d*Mn and *d*Fe in the CoFeMUG section (Noble et al., 2012; Saito et
699 al., 2013). These new field observations, together with increased recognition of
700 organic metal-binding ligands in hydrothermal fluids (e.g., Sander et al., 2007;
701 Bennett et al., 2008; Toner et al., 2009; Sander and Koschinsky, 2011), have
702 overturned the previous assertion that mineral precipitation and scavenging
703 quantitatively remove Fe from hydrothermal plumes (e.g., German et al., 1991b).

704

705 Measurements of this study do not indicate any similar release of *d*REEs to the water-
706 column (Fig. 3). The deconvolution results also confirm this conclusion, and instead
707 quantify removal of *d*Nd above the mid-ocean ridge rather than addition. The lack of
708 *d*REE addition may be surprising, given that hydrothermal fluids are enriched in
709 *d*REEs by several orders of magnitude compared to ambient seawater (e.g.,
710 Klinkhammer et al., 1994; Mitra et al., 1994; Bau and Dulski, 1999; Douville et al.,
711 1999; Craddock et al., 2010; Schmidt et al., 2010), but is consistent with previous
712 studies indicating quantitative scavenging of *d*REEs in hydrothermal plumes (e.g.,
713 German et al., 1990; Mitra et al., 1994; Bau and Dulski, 1999). The removal of

LREEs observed here is also consistent with previous studies that have demonstrated preferential scavenging of LREEs on Fe-Mn particles during dispersion of particles in neutrally buoyant hydrothermal plumes (German et al., 1990; Rudnicki and Elderfield, 1993; Mitra et al., 1994).

5.5. Apparent decoupling between Ce and Mn in the Angola Basin

Cerium often behaves similarly to Mn in the ocean due to their similar redox potential (e.g., Moffett, 1994b). This is the case, for example, in the OMZ where elevated *d*Ce concentration coincides with high *d*Mn concentrations at the CoFeMUG section. This is not the case at ~1500 m near the Angolan margin, however, where the plume of high Ce concentrations and Ce anomaly values is not accompanied by parallel enrichment in *d*Mn (Noble et al., 2012). This mismatch indicates that some processes, besides inorganic oxidation–reduction, decouple the cycles of these two elements at this depth.

A similar decoupling between Ce and Mn, albeit of much smaller magnitude, was previously observed in the northwest Indian Ocean (German and Elderfield, 1990). This decoupling was attributed to a delicate environment where dO_2 concentrations are sufficiently high to allow for the oxidative precipitation of Mn at the sediment–seawater interface during diffusion of Mn from reduced sediments, but insufficient to cause oxidative removal of Ce from the same sedimentary source. This explanation, however, seems inconsistent with high *d*Fe concentrations observed at ~1500 m at the CoFeMUG section (Noble et al., 2012). Because the standard redox potential follows the sequence Fe<Mn<Ce (Lu et al., 2010), if reduced sediments on the continental

margin serve as a local source of these metals to the water column, enrichment of *d*Fe and *d*Ce at ~1500 m, but not *d*Mn, is inconsistent with the redox chemistry of these elements during their diffusion out of sediments. A possible explanation for this apparent inconsistency is that Mn content in sediments along the African continental margin is much lower relative to Fe (Bremner and Willis, 1993), so that the supply of Mn from the reduced sedimentary source would be intrinsically low. In addition, Ce may be present as cerium oxides, or be mostly associated with Fe oxides in sediments, rather than being associated with Mn oxides, as demonstrated previously by data from pore waters off Peru and California margins (Haley et al., 2004).

6. CONCLUSIONS

This study presents *d*REE concentrations along a full-depth, zonal section at ~12°S in the tropical South Atlantic. High *d*REE concentrations in surface waters and OMZ (~400 m) near the Angolan coast are likely to result at least partially from decomposition of Fe-Mn oxides in the water column.

The contribution of water mass mixing to *d*REE concentrations in deep waters (>1000 m) was quantified using a multi-parameter end-member mixing model. Results show that >75% of the *d*REE concentrations are preformed. This explains the observed strong correlation between *d*REEs and dissolved Si in the deep Brazil Basin; both elements behave almost conservatively in deep-waters of the Atlantic. The deconvolution also reveals *d*REE addition of up to ~10% in AABW in the deep Brazil Basin, which reflects remineralization of particulates *in-situ* or along the flow path from ~40°S. More significant *d*REE addition of up to 25% was found at ~1500 m and

764 below ~4000 m in the Angola Basin near the continent–ocean interface, the upper
765 associated with increased Ce anomalies values and the deeper not. The shallow plume
766 is attributed to release of *d*REEs from dissolution of sedimentary Fe oxides on the
767 continental margin, and the deep one to remineralization of calcite. The higher
768 percentage of *d*REE addition in the Angola Basin compared to that in the Brazil Basin
769 may reflect the higher particulate fluxes, together with older water masses and a more
770 sluggish circulation in the Angola Basin that permit accumulation of more non-
771 conservative *d*REEs during water mass advection from source regions. These
772 observations suggest that processes responsible for the boundary sources of REEs
773 differ significantly with region.
774
775 Hydrothermal venting at the MAR does not lead to a net *d*REE flux to the deep ocean,
776 despite injecting significant amount of *d*Fe and *d*Mn at this section. Instead, the
777 deconvolution indicates that the MAR acts as a net sink for *d*LREEs, and has
778 negligible effect on the *d*HREE budget.
779
780 **ACKNOWLEDGEMENTS**
781
782 We thank Abigail Noble for sub-sampling and shipping samples to Oxford, Chao Liu
783 for advice on developing the codes for REE deconvolution, and Jie Yang for helping
784 with sample preparation and stimulating discussions. X.-Y. Zheng was supported by
785 the Clarendon Scholarship, the Exeter College Mandarin Scholarship from University
786 of Oxford, the Chinese Student Awards from the Great Britain–China Educational
787 Trust (GBCET) and W Wing Yip and Brothers bursaries. Comments from Martin
788 Frank, Stuart Robinson, two anonymous reviewers and the editor Silke Severmann

have significantly improved the manuscript.

REFERENCES

Akagi T. (2013) Rare earth element (REE)–silicic acid complexes in seawater to explain the incorporation of REEs in opal and the "leftover" REEs in surface water: new interpretation of dissolved REE distribution profiles. *Geochim. Cosmochim. Acta* **113**, 174-192.

Akagi T., Fu F.-f., Hongo Y. and Takahashi K. (2011) Composition of rare earth elements in settling particles collected in the highly productive North Pacific Ocean and Bering Sea: implications for siliceous-matter dissolution kinetics and formation of two REE-enriched phases. *Geochim. Cosmochim. Acta* **75**, 4857-4876.

Alibo D. S. and Nozaki Y. (2004) Dissolved rare earth elements in the eastern Indian Ocean: chemical tracers of the water masses. *Deep Sea Res. Part I* **51**, 559-576.

Amakawa H., Sasaki K. and Ebihara M. (2009) Nd isotopic composition in the central North Pacific. *Geochim. Cosmochim. Acta* **73**, 4705-4719.

Arhan M., Mercier H. and Park Y.-H. (2003) On the deep water circulation of the eastern South Atlantic Ocean. *Deep Sea Res. Part I* **50**, 889-916.

Arsouze T., Dutay J. C., Lacan F. and Jeandel C. (2009) Reconstructing the Nd oceanic cycle using a coupled dynamical – biogeochemical model. *Biogeosciences* **6**, 2829-2846.

Bau M. and Dulski P. (1999) Comparing yttrium and rare earths in hydrothermal fluids from the Mid-Atlantic Ridge: implications for Y and REE behaviour during near-vent mixing and for the Y/Ho ratio of Proterozoic seawater. *Chem. Geol.* **155**, 77-90.

Bayon G., German C. R., Burton K. W., Nesbitt R. W. and Rogers N. (2004) Sedimentary Fe-Mn oxyhydroxides as paleoceanographic archives and the role of aeolian flux in regulating oceanic dissolved REE. *Earth Planet. Sci. Lett.* **224**, 477-492.

Bayon G., Birot D., Ruffine L., Caprais J. C., Ponzevera E., Bollinger C. et al. (2011) Evidence for intense REE scavenging at cold seeps from the Niger Delta margin. *Earth Planet. Sci. Lett.* **312**, 443-452.

Bennett S. A., Achterberg E. P., Connelly D. P., Statham P. J., Fones G. R. and German C. R. (2008) The distribution and stabilisation of dissolved Fe in deep-sea hydrothermal plumes. *Earth Planet. Sci. Lett.* **270**, 157-167.

Bertram C. J. and Elderfield H. (1993) The geochemical balance of the rare earth elements and neodymium isotopes in the oceans. *Geochim. Cosmochim. Acta* **57**, 1957-1986.

Borradaile G. J. (2003) Statistics of earth science data: their distribution in time, space and orientation. Springer.

Bremner J. M. and Willis J. P. (1993) Mineralogy and geochemistry of the clay fraction of sediments from the Namibian continental margin and the adjacent hinterland. *Mar. Geol.* **115**, 85-116.

Broecker W. S., Blanton S., Smethie W. M. and Ostlund G. (1991) Radiocarbon decay and oxygen utilization in the Deep Atlantic Ocean. *Global Biogeochem. Cycles* **5**, 87-117.

Byrne R. and Sholkovitz E. (1996) Marine chemistry and geochemistry of the lanthanides. In *Handbook on the physics and chemistry of rare earths* (eds. K. A. Gschneidner Jr. and L. Eyring.) Elsevier, 497-593.

Byrne R. H. and Kim K.-H. (1990) Rare earth element scavenging in seawater. *Geochim. Cosmochim. Acta* **54**, 2645-2656.

Carter P., Vance D., Hillenbrand C. D., Smith J. A. and Shoosmith D. R. (2012) The neodymium isotopic composition of waters masses in the eastern Pacific sector of the Southern Ocean. *Geochim. Cosmochim. Acta* **79**, 41-59.

Craddock P. R., Bach W., Seewald J. S., Rouxel O. J., Reeves E. and Tivey M. K. (2010) Rare earth element abundances in hydrothermal fluids from the Manus Basin, Papua New Guinea: indicators of sub-seafloor hydrothermal processes in back-arc basins. *Geochim. Cosmochim. Acta* **74**, 5494-5513.

de Baar H. J. W., Bacon M. P. and Brewer P. G. (1983) Rare-earth distributions with a positive Ce anomaly in the Western North Atlantic Ocean. *Nature* **301**, 324-327.

de Baar H. J. W., Bacon M. P., Brewer P. G. and Bruland K. W. (1985) Rare earth elements in the Pacific and Atlantic Oceans. *Geochim. Cosmochim. Acta* **49**, 1943-1959.

de Baar H. J. W., German C. R., Elderfield H. and van Gaans P. (1988) Rare earth element distributions in anoxic waters of the Cariaco Trench. *Geochim. Cosmochim. Acta* **52**, 1203-1219.

Douville E., Bienvenu P., Charlou J. L., Donval J. P., Fouquet Y., Appriou P. et al. (1999) Yttrium and rare earth elements in fluids from various deep-sea hydrothermal systems. *Geochim. Cosmochim. Acta* **63**, 627-643.

Elderfield H. and Greaves M. J. (1982) The rare earth elements in seawater. *Nature* **296**, 214-219.

Elderfield H., Whitfield M., Burton J. D., Bacon M. P. and Liss P. S. (1988) The oceanic chemistry of the rare-earth elements. *Philosophical Transactions of the Royal Society A: Mathematical and Physical Sciences* **325**, 105-126.

Feely R. A., Sabine C. L., Lee K., Berelson W., Kleypas J., Fabry V. J. et al. (2004) Impact of Anthropogenic CO2 on the CaCO3 System in the Oceans. *Science* **305**, 362-366.

Fitzsimmons J. N., Boyle E. A. and Jenkins W. J. (2014) Distal transport of dissolved hydrothermal iron in the deep South Pacific Ocean. *Proceedings of the National Academy of Sciences* **111**, 16654-16661.

Freslon N., Bayon G., Toucanne S., Bermell S., Bollinger C., Chéron S. et al. (2014) Rare earth elements and neodymium isotopes in sedimentary organic matter. *Geochim. Cosmochim. Acta* **140**, 177-198.

Garcia-Solsona E., Jeandel C., Labatut M., Lacan F., Vance D., Chavagnac V. et al. (2014) Rare earth elements and Nd isotopes tracing water mass mixing and particle-seawater interactions in the SE Atlantic. *Geochim. Cosmochim. Acta* **125**, 351-372.

German C. R. and Elderfield H. (1989) Rare earth elements in Saanich Inlet, British Columbia, a seasonally anoxic basin. *Geochim. Cosmochim. Acta* **53**, 2561-2571.

German C. R. and Elderfield H. (1990) Rare earth elements in the NW Indian Ocean. *Geochim. Cosmochim. Acta* **54**, 1929-1940.

German C. R., Holliday B. P. and Elderfield H. (1991a) Redox cycling of rare earth elements in the suboxic zone of the Black Sea. *Geochim. Cosmochim. Acta* **55**, 3553-3558.

German C. R., Campbell A. C. and Edmond J. M. (1991b) Hydrothermal scavenging at the Mid-Atlantic Ridge: modification of trace element dissolved fluxes. *Earth Planet. Sci. Lett.* **107**, 101-114.

German C. R., Klinkhammer G. P., Edmond J. M., Mura A. and Elderfield H. (1990) Hydrothermal scavenging of rare-earth elements in the ocean. *Nature* **345**, 516-518.

German C. R., Masuzawa T., Greaves M. J., Elderfield H. and Edmond J. M. (1995) Dissolved rare earth elements in the Southern Ocean: cerium oxidation and the influence of hydrography. *Geochim. Cosmochim. Acta* **59**, 1551-1558.

Goldstein S. L. and Hemming S. R. (2003) Long-lived Isotopic tracers in oceanography, paleoceanography, and ice-sheet dynamics. In *Treatise on Geochemistry* (ed. H. Elderfield.) Pergamon, Oxford. pp. 453-489.

Goswami V., Singh S. K. and Bhushan R. (2014) Impact of water mass mixing and dust deposition on Nd concentration and ε_{Nd} of the Arabian Sea water column. *Geochim. Cosmochim. Acta* **145**, 30-49.

Grasse P., Stichel T., Stumpf R., Stramma L. and Frank M. (2012) The distribution of neodymium isotopes and concentrations in the Eastern Equatorial Pacific: water mass advection versus particle exchange. *Earth Planet. Sci. Lett.* **353–354**, 198-207.

Greaves M. J., Statham P. J. and Elderfield H. (1994) Rare earth element mobilization from marine atmospheric dust into seawater. *Mar. Chem.* **46**, 255-260.

Grenier M., Jeandel C., Lacan F., Vance D., Venchiarutti C., Cros A. et al. (2013) From the subtropics to the central equatorial Pacific Ocean: Neodymium isotopic composition and rare earth element concentration variations. *Journal of Geophysical Research: Oceans* **118**, 592-618.

Haley B. A., Klinkhammer G. P. and McManus J. (2004) Rare earth elements in pore waters of marine sediments. *Geochim. Cosmochim. Acta* **68**, 1265-1279.

Haley B. A., Klinkhammer G. P. and Mix A. C. (2005) Revisiting the rare earth elements in foraminiferal tests. *Earth Planet. Sci. Lett.* **239**, 79-97.

Haley B. A., Frank M., Hathorne E. and Pisias N. (2014) Biogeochemical implications from dissolved rare earth element and Nd isotope distributions in the Gulf of Alaska. *Geochim. Cosmochim. Acta* **126**, 455-474.

Hathorne E. C., Stichel T., Brück B. and Frank M. (2015) Rare earth element distribution in the Atlantic sector of the Southern Ocean: The balance between particle scavenging and vertical supply. *Mar. Chem.* **177,** 157-171.

Hatta M. and Zhang J. (2006) Possible source of advected water mass and residence times in the multi-structured Sea of Japan using rare earth elements. *Geophys. Res. Lett.* **33**, L16606.

Hatta M., Measures C. I., Wu J., Roshan S., Fitzsimmons J. N., Sedwick P. and Morton P. (2015) An overview of dissolved Fe and Mn distributions during the 2010–2011 U.S. GEOTRACES north Atlantic cruises: GEOTRACES GA03. *Deep Sea Res. Part II* **116**, 117-129.

Henson S. A., Sanders R. and Madsen E. (2012) Global patterns in efficiency of particulate organic carbon export and transfer to the deep ocean. *Global Biogeochem. Cycles* **26**, GB1028.

Hupe A. and Karstensen J. (2000) Redfield stoichiometry in Arabian Sea subsurface waters. *Global Biogeochem. Cycles* **14**, 357-372.

Jeandel C. (1993) Concentration and isotopic composition of Nd in the South Atlantic Ocean. *Earth Planet. Sci. Lett.* **117**, 581-591.

Jeandel C., Arsouze T., Lacan F., Téchiné P. and Dutay J.-C. (2007) Isotopic Nd compositions and concentrations of the lithogenic inputs into the ocean: a compilation, with an emphasis on the margins. *Chem. Geol.* **239**, 156-164.

Jeandel C., Delattre H., Grenier M., Pradoux C. and Lacan F. (2013) Rare earth element concentrations and Nd isotopes in the Southeast Pacific Ocean. *Geochem. Geophys. Geosyst.* **14**, 328-341.

Johannesson K. H., Chevis D. A., Burdige D. J., Cable J. E., Martin J. B. and Roy M. (2011) Submarine groundwater discharge is an important net source of light and middle REEs to coastal waters of the Indian River Lagoon, Florida, USA. *Geochim. Cosmochim. Acta* **75**, 825-843.

Karstensen J. and Tomczak M. (1998) Age determination of mixed water masses using CFC and oxygen data. *Journal of Geophysical Research: Oceans* **103**, 18599-18609.

Klinkhammer G. P., Elderfield H., Edmond J. M. and Mitra A. (1994) Geochemical implications of rare earth element patterns in hydrothermal fluids from mid-ocean ridges. *Geochim. Cosmochim. Acta* **58**, 5105-5113.

Klunder M. B., Laan P., Middag R., de Baar H. J. W. and Bakker K. (2012) Dissolved iron in the Arctic Ocean: Important role of hydrothermal sources, shelf input and scavenging removal. *Journal of Geophysical Research: Oceans* **117**, C04014.

Lacan F. and Jeandel C. (2004) Subpolar Mode Water formation traced by neodymium isotopic composition. *Geophys. Res. Lett.* **31**.

Lacan F. and Jeandel C. (2005a) Neodymium isotopes as a new tool for quantifying exchange fluxes at the continent-ocean interface. *Earth Planet. Sci. Lett.* **232**, 245-257.

Lacan F. and Jeandel C. (2005b) Acquisition of the neodymium isotopic composition of the North Atlantic Deep Water. *Geochemistry Geophysics Geosystems* **6**.

Lambelet M., van de Flierdt T., Crocket K., Rehkämper M., Kreissig K., Coles B., Rijkenberg M. J. A., Gerringa L. J. A., de Baar H. J. W. and Steinfeldt R. (2016) Neodymium isotopic composition and concentration in the western North Atlantic Ocean: results from the GEOTRACES GA02 section. *Geochim. Cosmochim. Acta*, in press.

Larqué L., Maamaatuaiahutapu K. and Garçon V. (1997) On the intermediate and deep water flows in the South Atlantic Ocean. *Journal of Geophysical Research: Oceans* **102**, 12425-12440.

Lass H. U. and Mohrholz V. (2008) On the interaction between the subtropical gyre and the Subtropical Cell on the shelf of the SE Atlantic. *Journal of Marine Systems* **74**, 1-43.

Lee K., Choi S. D., Park G. H., Wanninkhof R., Peng T. H., Key R. M. et al. (2003) An updated anthropogenic CO2 inventory in the Atlantic Ocean. *Global Biogeochem. Cycles* **17**, 1116.

Lu Z. L., Jenkyns H. C. and Rickaby R. E. M. (2010) Iodine to calcium ratios in marine carbonate as a paleo-redox proxy during oceanic anoxic events. *Geology* **38**, 1107-1110.

Marsh R. (2000) Recent Variability of the North Atlantic Thermohaline Circulation Inferred from Surface Heat and Freshwater Fluxes. *J. Clim.* **13**, 3239-3260.

Mawji E., Schlitzer R., Dodas E. M., Abadie C., Abouchami W., Anderson R. F. et al. (2015) The GEOTRACES Intermediate Data Product 2014. *Mar. Chem.*

McLennan S. M. (1989) Rare earth elements in sedimentary rocks; influence of provenance and sedimentary processes. *Rev. Mineral. Geochem.* **21**, 169-200.

Mercier H., Arhan M. and Lutjeharms J. R. E. (2003) Upper-layer circulation in the eastern Equatorial and South Atlantic Ocean in January–March 1995. *Deep Sea Res. Part I* **50**, 863-887.

Mitra A., Elderfield H. and Greaves M. J. (1994) Rare earth elements in submarine hydrothermal fluids and plumes from the Mid-Atlantic Ridge. *Mar. Chem.* **46**, 217-235.

Moffett J. W. (1990) Microbially mediated cerium oxidation in sea water. *Nature* **345**, 421-423.

Moffett J. W. (1994a) A radiotracer study of cerium and manganese uptake onto suspended particles in Chesapeake Bay. *Geochim. Cosmochim. Acta* **58**, 695-703.

Moffett J. W. (1994b) The relationship between cerium and manganese oxidation in the marine environment. *Limnol. Oceanogr.* **39**, 1309-1318.

Mohrholz V., Bartholomae C. H., van der Plas A. K. and Lass H. U. (2008) The seasonal variability of

964 the northern Benguela undercurrent and its relation to the oxygen budget on the shelf. *Cont.*
965 *Shelf Res.* **28**, 424-441.
966 Molina-Kescher M., Frank M. and Hathorne E. (2014) South Pacific dissolved Nd isotope
967 compositions and rare earth element distributions: water mass mixing versus biogeochemical
968 cycling. *Geochim. Cosmochim. Acta* **127**, 171-189.
969 Nishioka J., Obata H. and Tsumune D. (2013) Evidence of an extensive spread of hydrothermal
970 dissolved iron in the Indian Ocean. *Earth Planet. Sci. Lett.* **361**, 26-33.
971 Noble A. E., Lamborg C. H., Ohnemus D. C., Lam P. J., Goepfert T. J., Measures C. I. et al. (2012)
972 Basin-scale inputs of cobalt, iron, and manganese from the Benguela-Angola front to the
973 South Atlantic Ocean. *Limnol. Oceanogr.* **57**, 989-1010.
974 Nozaki Y. and Alibo D. S. (2003) Importance of vertical geochemical processes in controlling the
975 oceanic profiles of dissolved rare earth elements in the northeastern Indian Ocean. *Earth*
976 *Planet. Sci. Lett.* **205**, 155-172.
977 Nozaki Y., Alibo D.-S., Amakawa H., Gamo T. and Hasumoto H. (1999) Dissolved rare earth elements
978 and hydrography in the Sulu Sea. *Geochim. Cosmochim. Acta* **63**, 2171-2181.
979 Palmer M. R. (1985) Rare earth elements in foraminifera tests. *Earth Planet. Sci. Lett.* **73**, 285-298.
980 Pearce C. R., Jones M. T., Oelkers E. H., Pradoux C. and Jeandel C. (2013) The effect of particulate
981 dissolution on the neodymium (Nd) isotope and rare earth element (REE) composition of
982 seawater. *Earth Planet. Sci. Lett.* **369–370**, 138-147.
983 Pickart R. S., Spall M. A. and Lazier J. R. N. (1997) Mid-depth ventilation in the western boundary
984 current system of the sub-polar gyre. *Deep Sea Res. Part I* **44**, 1025-1054.
985 Pickart R. S., Smethie W. M., Lazier J. R. N., Jones E. P. and Jenkins W. J. (1996) Eddies of newly
986 formed upper Labrador Sea water. *Journal of Geophysical Research: Oceans* **101**, 20711-
987 20726.
988 Piepgras D. J. and Wasserburg G. J. (1983) Influence of the Mediterranean Outflow on the isotopic
989 composition of neodymium in waters of the North Atlantic. *Journal of Geophysical Research:*
990 *Oceans* **88**, 5997-6006.
991 Piepgras D. J. and Wasserburg G. J. (1987) Rare earth element transport in the western North Atlantic
992 inferred from Nd isotopic observations. *Geochim. Cosmochim. Acta* **51**, 1257-1271.
993 Rempfer J., Stocker T. F., Joos F., Dutay J.-C. and Siddall M. (2011) Modelling Nd-isotopes with a
994 coarse resolution ocean circulation model: sensitivities to model parameters and source/sink
995 distributions. *Geochim. Cosmochim. Acta* **75**, 5927-5950.
996 Resing J. A., Sedwick P. N., German C. R., Jenkins W. J., Moffett J. W., Sohst B. M. and Tagliabue A.
997 (2015) Basin-scale transport of hydrothermal dissolved metals across the South Pacific Ocean.
998 *Nature* **523**, 200-203.
999 Rhein M., Stramma L. and Send U. (1995) The Atlantic Deep Western Boundary Current: water masses
1000 and transports near the equator. *Journal of Geophysical Research: Oceans* **100**, 2441-2457.
1001 Rickli J., Frank M. and Halliday A. N. (2009) The hafnium-neodymium isotopic composition of
1002 Atlantic seawater. *Earth Planet. Sci. Lett.* **280**, 118-127.
1003 Rickli J., Frank M., Baker A. R., Aciego S., de Souza G., Georg R. B. et al. (2010) Hafnium and
1004 neodymium isotopes in surface waters of the eastern Atlantic Ocean: implications for sources
1005 and inputs of trace metals to the ocean. *Geochim. Cosmochim. Acta* **74**, 540-557.
1006 Rudnicki M. D. and Elderfield H. (1993) A chemical model of the buoyant and neutrally buoyant
1007 plume above the TAG vent field, 26 degrees N, Mid-Atlantic Ridge. *Geochim. Cosmochim.*
1008 *Acta* **57**, 2939-2957.
1009 Saito M. A., Noble A. E., Tagliabue A., Goepfert T. J., Lamborg C. H. and Jenkins W. J. (2013) Slow-
1010 spreading submarine ridges in the South Atlantic as a significant oceanic iron source. *Nature*
1011 *Geosci* **6**, 775-779.
1012 Sander S. G. and Koschinsky A. (2011) Metal flux from hydrothermal vents increased by organic
1013 complexation. *Nature Geosci* **4**, 145-150.
1014 Sander S. G., Koschinsky A., Massoth G., Stott M. and Hunter K. A. (2007) Organic complexation of
1015 copper in deep-sea hydrothermal vent systems. *Environmental Chemistry* **4**, 81-89.
1016 Sarmiento J. L., Simeon J., Gnanadesikan A., Gruber N., Key R. M. and Schlitzer R. (2007) Deep
1017 ocean biogeochemistry of silicic acid and nitrate. *Global Biogeochem. Cycles* **21**, GB1S90.
1018 Schijf J., de Baar H. J. W. and Millero F. J. (1995) Vertical distributions and speciation of dissolved
1019 rare earth elements in the anoxic brines of Bannock Basin, eastern Mediterranean Sea.
1020 *Geochim. Cosmochim. Acta* **59**, 3285-3299.
1021 Schmidt K., Garbe-Schönberg D., Bau M. and Koschinsky A. (2010) Rare earth element distribution
1022 in >400°C hot hydrothermal fluids from 5°S, MAR: The role of anhydrite in controlling
1023 highly variable distribution patterns. *Geochim. Cosmochim. Acta* **74**, 4058-4077.

Sholkovitz E. R. and Schneider D. L. (1991) Cerium redox cycles and rare earth elements in the Sargasso Sea. *Geochim. Cosmochim. Acta* **55**, 2737-2743.
Sholkovitz E. R., Shaw T. J. and Schneider D. L. (1992) The geochemistry of rare earth elements in the seasonally anoxic water column and porewaters of Chesapeake Bay. *Geochim. Cosmochim. Acta* **56**, 3389-3402.
Sholkovitz E. R., Landing W. M. and Lewis B. L. (1994) Ocean particle chemistry: the fractionation of rare earth elements between suspended particles and seawater. *Geochim. Cosmochim. Acta* **58**, 1567-1579.
Siddall M., Khatiwala S., van de Flierdt T., Jones K., Goldstein S. L., Hemming S. et al. (2008) Towards explaining the Nd paradox using reversible scavenging in an ocean general circulation model. *Earth Planet. Sci. Lett.* **274**, 448-461.
Singh S. P., Singh S. K., Goswami V., Bhushan R. and Rai V. K. (2012) Spatial distribution of dissolved neodymium and ε_{Nd} in the Bay of Bengal: role of particulate matter and mixing of water masses. *Geochim. Cosmochim. Acta* **94**, 38-56.
Smethie W. M., Fine R. A., Putzka A. and Jones E. P. (2000) Tracing the flow of North Atlantic Deep Water using chlorofluorocarbons. *Journal of Geophysical Research: Oceans* **105**, 14297-14323.
Stichel T., Frank M., Rickli J. and Haley B. A. (2012a) The hafnium and neodymium isotope composition of seawater in the Atlantic sector of the Southern Ocean. *Earth Planet. Sci. Lett.* **317–318**, 282-294.
Stichel T., Hartman A. E., Duggan B., Goldstein S. L., Scher H. and Pahnke K. (2015) Separating biogeochemical cycling of neodymium from water mass mixing in the Eastern North Atlantic. *Earth Planet. Sci. Lett.* **412**, 245-260.
Stichel T., Frank M., Rickli J., Hathorne E. C., Haley B. A., Jeandel C. et al. (2012b) Sources and input mechanisms of hafnium and neodymium in surface waters of the Atlantic sector of the Southern Ocean. *Geochim. Cosmochim. Acta* **94**, 22-37.
Stramma L. and England M. (1999) On the water masses and mean circulation of the South Atlantic Ocean. *J. Geophys. Res.* **104**, 20863-20883.
Tachikawa K., Athias V. and Jeandel C. (2003) Neodymium budget in the modern ocean and paleo-oceanographic implications. *Journal of Geophysical Research-Oceans* **108**,
Takeda S. (1998) Influence of iron availability on nutrient consumption ratio of diatoms in oceanic waters. *Nature* **393**, 774-777.
Tarantola A. (2005) Inverse problem theory and methods for model parameter estimation. Society for Industrial and Applied Mathematics, Philadelphia.
Tebo B. M., Bargar J. R., Clement B. G., Dick G. J., Murray K. J., Parker D. et al. (2004) BIOGENIC MANGANESE OXIDES: Properties and Mechanisms of Formation. *Annual Review of Earth and Planetary Sciences* **32**, 287-328.
Tomczak M. and Large D. G. B. (1989) Optimum multiparameter analysis of mixing in the thermocline of the eastern Indian Ocean. *Journal of Geophysical Research: Oceans* **94**, 16141-16149.
Toner B. M., Fakra S. C., Manganini S. J., Santelli C. M., Marcus M. A., Moffett J. W. et al. (2009) Preservation of iron(II) by carbon-rich matrices in a hydrothermal plume. *Nature Geosci* **2**, 197-201.
van de Flierdt T., Pahnke K., Amakawa H., Andersson P., Basak C., Coles B. et al. (2012) GEOTRACES intercalibration of neodymium isotopes and rare earth element concentrations in seawater and suspended particles. Part 1: reproducibility of results for the international intercomparison. *Limnology and Oceanography-Methods* **10**, 234-251.
Vanicek M. and Siedler G. (2002) Zonal Fluxes in the Deep Water Layers of the Western South Atlantic Ocean. *J. Phys. Oceanogr.* **32**, 2205-2235.
Warren B. A. and Speer K. G. (1991) Deep circulation in the eastern South Atlantic Ocean. *Deep Sea Research Part A. Oceanographic Research Papers* **38**, S281-S322.
Wienders N., Arhan M. and Mercier H. (2000) Circulation at the western boundary of the South and Equatorial Atlantic: Exchanges with the ocean interior. *J. Mar. Res.* **58**, 1007-1039.
Wood S. A. (1990) The aqueous geochemistry of the rare-earth elements and yttrium: 1. review of available low-temperature data for inorganic complexes and the inorganic REE speciation of natural waters. *Chem. Geol.* **82**, 159-186.
Zhang J. and Nozaki Y. (1996) Rare earth elements and yttrium in seawater: ICP-MS determinations in the East Caroline, Coral Sea, and South Fiji basins of the western South Pacific Ocean. *Geochim. Cosmochim. Acta* **60**, 4631-4644.
Zhang J. and Nozaki Y. (1998) Behavior of rare earth elements in seawater at the ocean margin: a study along the slopes of the Sagami and Nankai troughs near Japan. *Geochim. Cosmochim. Acta* **62**,

1307-1317.
Zhang Y., Lacan F. and Jeandel C. (2008) Dissolved rare earth elements tracing lithogenic inputs over the Kerguelen Plateau (Southern Ocean). *Deep Sea Res. Part II* **55**, 638-652.
Zheng X.-Y., Yang J. and Henderson G. M. (2015) A robust procedure for high-precision determination of rare earth element concentrations in seawater. *Geostand. Geoanal. Res.* **39**, 277-292.

Fig. 1. Map showing the sampling stations of the CoFeMUG cruise (red circles), and the schematic flow patterns of major water masses affecting the region, based on Stramma and England (1999). Blue lines indicate surface-ocean circulation; orange lines denote North Atlantic Deep Water (NADW); yellow dashed lines represent Antarctic Bottom Water (AABW). SSEC: southern branches of the South Equatorial Current; ABF: Angola–Benguela Front.

Fig. 2. (A) Dissolved silicate (*d*Si) along the CoFeMUG section (Noble et al., 2012), and depth ranges of major water masses according to characteristic neutral density surfaces (Vanicek and Siedler, 2002). TSW–Tropical Surface Water; SACW–South Atlantic Central Water; AAIW–Antarctic Intermediate Water; UCDW–Upper Circumpolar Deep Water; NADW–North Atlantic Deep Water; AABW–Antarctic Bottom Water. Numbers above section are CoFeMUG station numbers (Fig. 1). (B) Dissolved O_2 showing the OMZ on the Angolan margin (Noble et al., 2012).

Fig. 3. Measured *d*Nd, *d*Yb, *d*Ce concentrations and Ce anomaly (Ce/Ce^*) along the CoFeMUG section. Numbers above section are CoFeMUG station numbers (Fig. 1). Figures were created using Ocean Data View (Schlitzer, R., Ocean Data View, odv.awi.de, 2015).

Fig. 4. Shale-normalized REE patterns from typical stations on either side of the section (Station 4 and 15).

Fig. 5. Results of modelled mixing fractions of UCDW, NADW (combined UNADW and LNADW) and AABW along the CoFeMUG section. Plotted results are the

arithmetic average of 250,000 Monte Carlo perturbation experiments. Figures were created using Ocean Data View (Schlitzer, R., Ocean Data View, odv.awi.de, 2015).

Fig. 6. Modelled mean ΔNd (A) and ΔYb (B) results over 250,000 perturbation experiments in pmol/kg for depths below 1000 m. Positive values reflect addition of Nd or Yb, while negative values reflect removal, relative to conservative mixing of the water-mass end-members. Figures were created using Ocean Data View (Schlitzer, R., Ocean Data View, odv.awi.de, 2015).

Fig. 7. Modelled ΔNd (A) and ΔYb (B) relative to respective total dissolved concentrations for depths below 1000 m. Positive values reflect addition of Nd or Yb, while negative values reflect removal. Figures were created using Ocean Data View (Schlitzer, R., Ocean Data View, odv.awi.de, 2015).

Fig. 8. Probability distribution characterizing the stability of the spatial patterns of ΔNd and ΔYb. The white dashed line shows the probability equal to 1/3 – the limit of statistical significance. Figures were created using Ocean Data View (Schlitzer, R., Ocean Data View, odv.awi.de, 2015).

Fig. 9. *d*REE (Ce anomaly)–*d*Fe (*d*Mn) correlations at ~400 m. Significant linear relationships between *d*REEs and *d*Fe or *d*Mn were observed within the OMZ (orange), but not for stations outside the OMZ (black; $dO_2 > \sim 60$ μM).

Fig. 10. REE patterns normalized against the average of REE concentrations at ~1000 m at the CoFeMUG section. (A) Seawater measurements from this study from

~400 m, with samples outside the OMZ shaded in grey. Note the LREE and Ce enrichment for samples in the OMZ, consistent with release of REEs from Fe-Mn oxides. (B) Fe-Mn leachate from sediments in the Angola Basin (Bayon et al., 2004), demonstrating expected patterns of REEs from dissolution of Fe-Mn oxides.

Fig. 11. Deep-water (>2000 m) *d*REE–*d*Si relationship in the Brazil and Angola Basin.

Table 1. Characteristics of each tracer in the 4 pre-defined end-member water types

		T (°C)[1]	S[1]	Silicate (µmol/L)[1]	Phosphate (µmol/L)[1]	*d*Nd (pmol/kg)[1]	*d*Yb (pmol/kg)[1]
UCDW		3.32 ± 0.52	34.51 ± 0.10	44.57 ± 8.84	2.22 ± 0.11	12.09 ± 0.96	5.37 ± 0.37
NADW	UNADW	4.21 ± 1.38	35.02 ± 0.22	12.01 ± 1.82	1.14 ± 0.06	16.89 ± 5.07	4.50 ± 0.41
	LNADW	2.61 ± 0.38	34.93 ± 0.03	24.94 ± 10.66	1.26 ± 0.16	19.17 ± 5.59	4.98 ± 0.53
AABW		0.49 ± 0.51	34.71 ± 0.04	113.47 ± 14.40	2.14 ± 0.14	32.20 ± 4.85	7.86 ± 0.98

[1] see text for details on how end-member values were defined and on references cited.

Figure_01

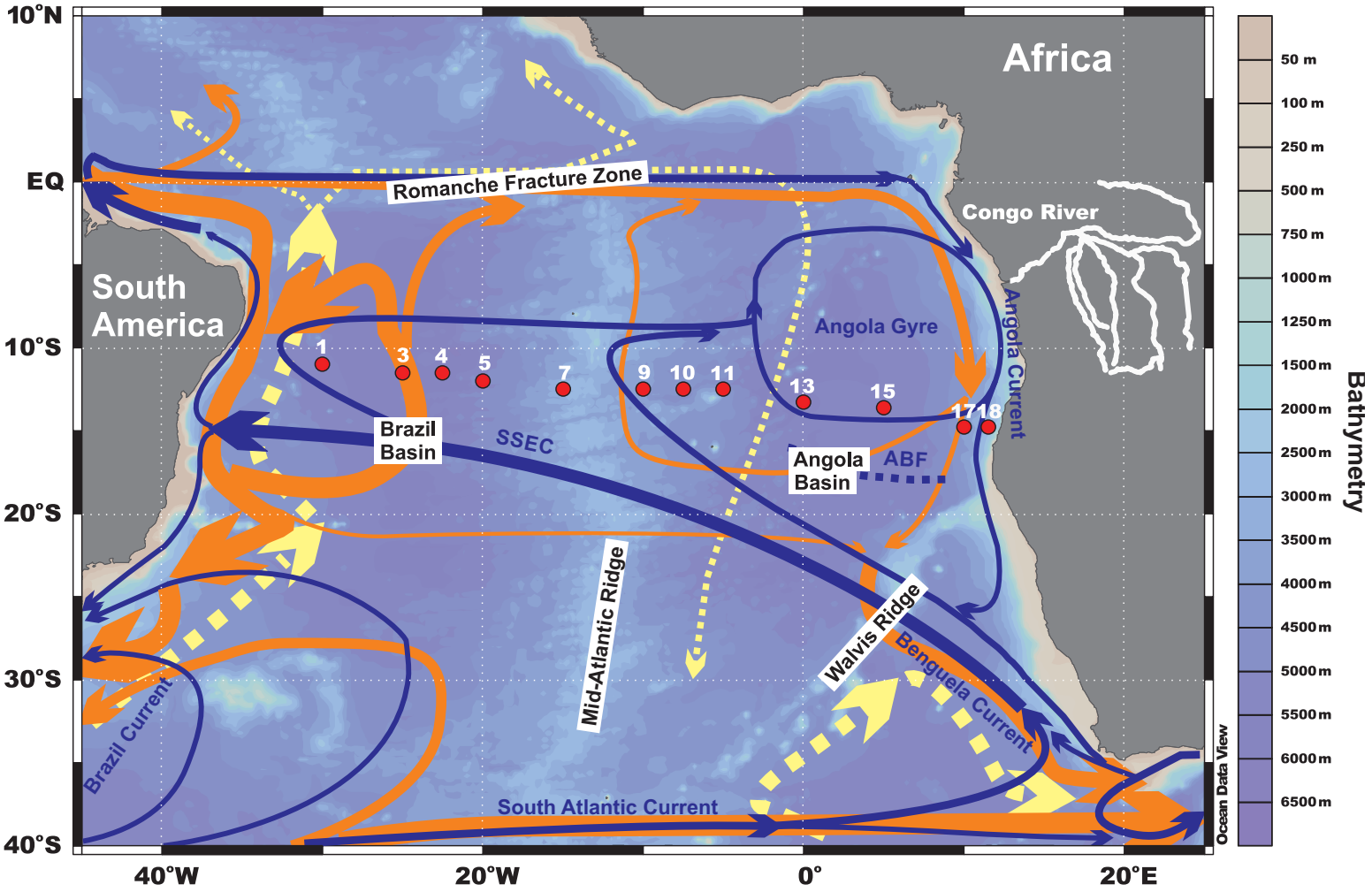
10°N
EQ
10°S
20°S
30°S
40°S
40°W
20°W
0°
20°E
Africa
South America
Romanche Fracture Zone
Congo River
Angola Gyre
Angola Current
Brazil Basin
SSEC
Angola Basin
ABF
Mid-Atlantic Ridge
Walvis Ridge
Benguela Current
Brazil Current
South Atlantic Current
1
3
4
5
7
9
10
11
13
15
17
18
Bathymetry
50 m
100 m
250 m
500 m
750 m
1000 m
1250 m
1500 m
2000 m
2500 m
3000 m
3500 m
4000 m
4500 m
5000 m
5500 m
6000 m
6500 m
Ocean Data View

Figure_02

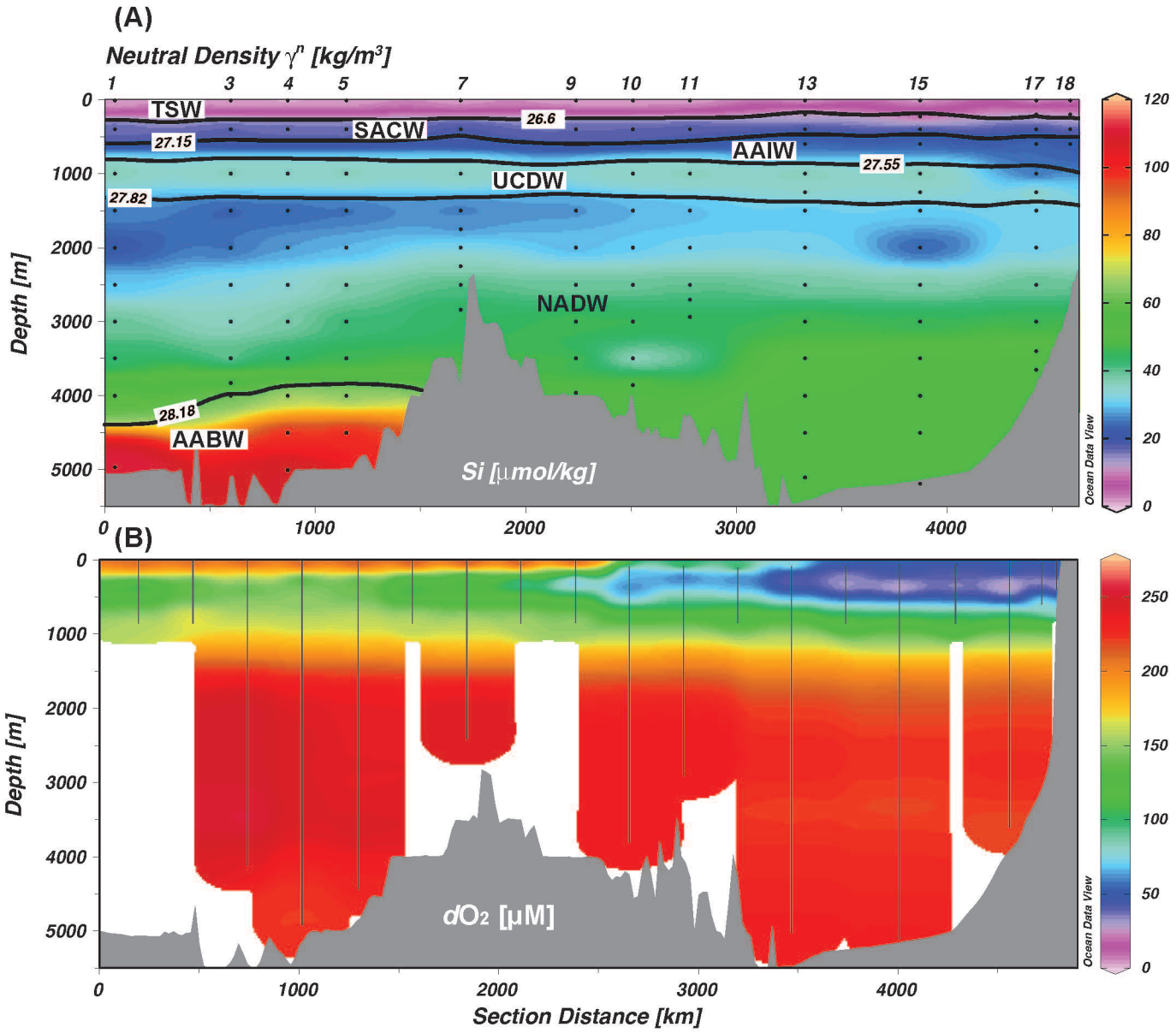
(A)
Neutral Density γ^n [kg/m^3]
1
3
4
5
7
9
10
11
13
15
17
18
TSW
SACW
AAIW
UCDW
NADW
AABW
26.6
27.15
27.55
27.82
28.18
Depth [m]
Si [µmol/kg]
Ocean Data View
(B)
dO2 [µM]
Section Distance [km]

Figure_03

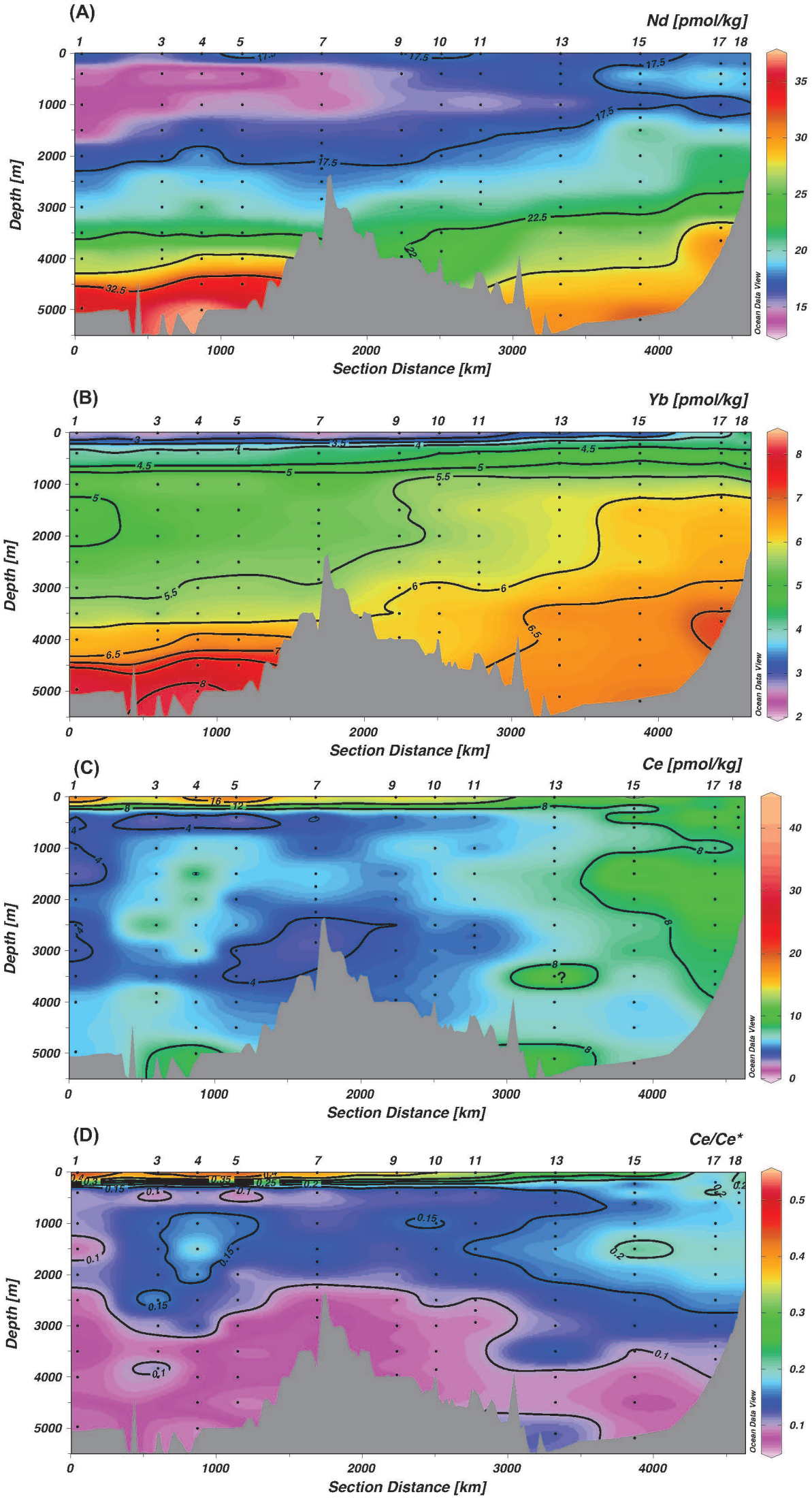
(A)
Nd [pmol/kg]
(B)
Yb [pmol/kg]
(C)
Ce [pmol/kg]
(D)
Ce/Ce*
Depth [m]
Section Distance [km]
Ocean Data View

Figure_04

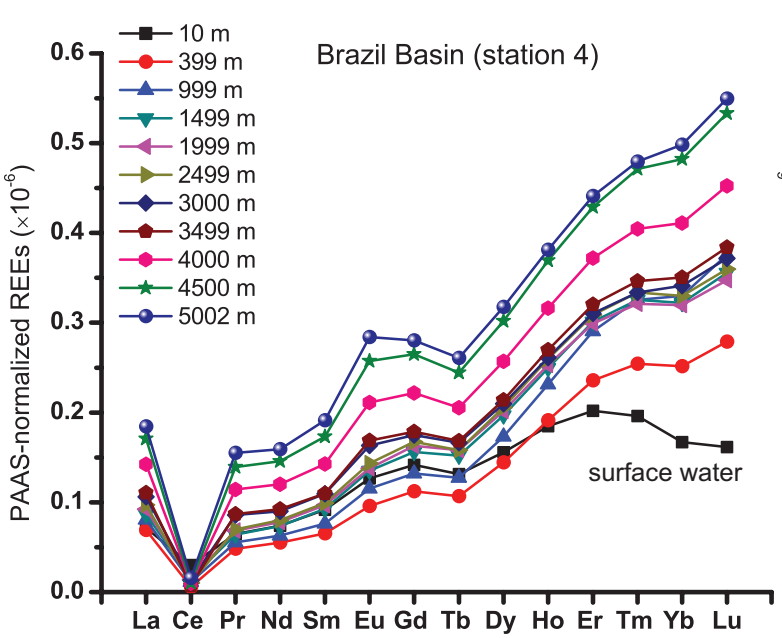
Brazil Basin (station 4)
10 m
399 m
999 m
1499 m
1999 m
2499 m
3000 m
3499 m
4000 m
4500 m
5002 m
surface water
PAAS-normalized REEs (×10-6)
0.0
0.1
0.2
0.3
0.4
0.5
0.6
La Ce Pr Nd Sm Eu Gd Tb Dy Ho Er Tm Yb Lu

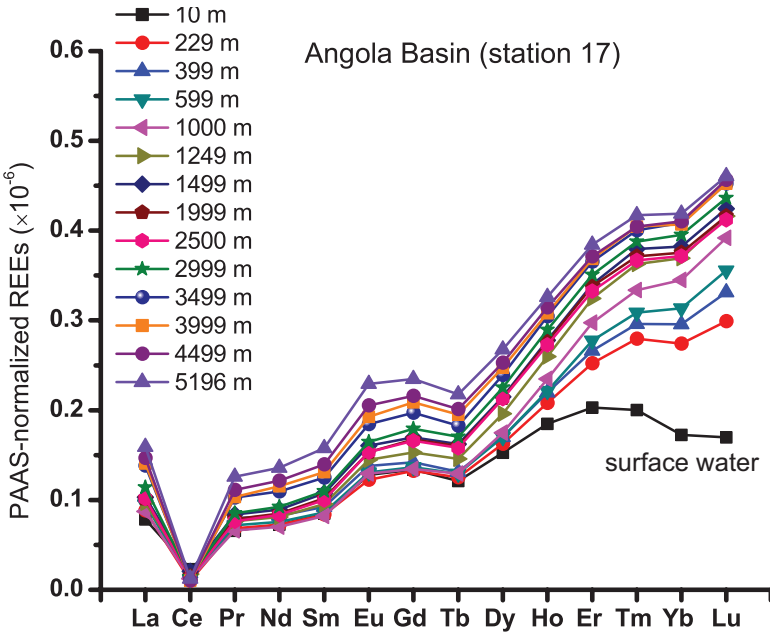
Angola Basin (station 17)
10 m
229 m
399 m
599 m
1000 m
1249 m
1499 m
1999 m
2500 m
2999 m
3499 m
3999 m
4499 m
5196 m
surface water
PAAS-normalized REEs (×10-6)
0.0
0.1
0.2
0.3
0.4
0.5
0.6
La Ce Pr Nd Sm Eu Gd Tb Dy Ho Er Tm Yb Lu

Figure_05_revised

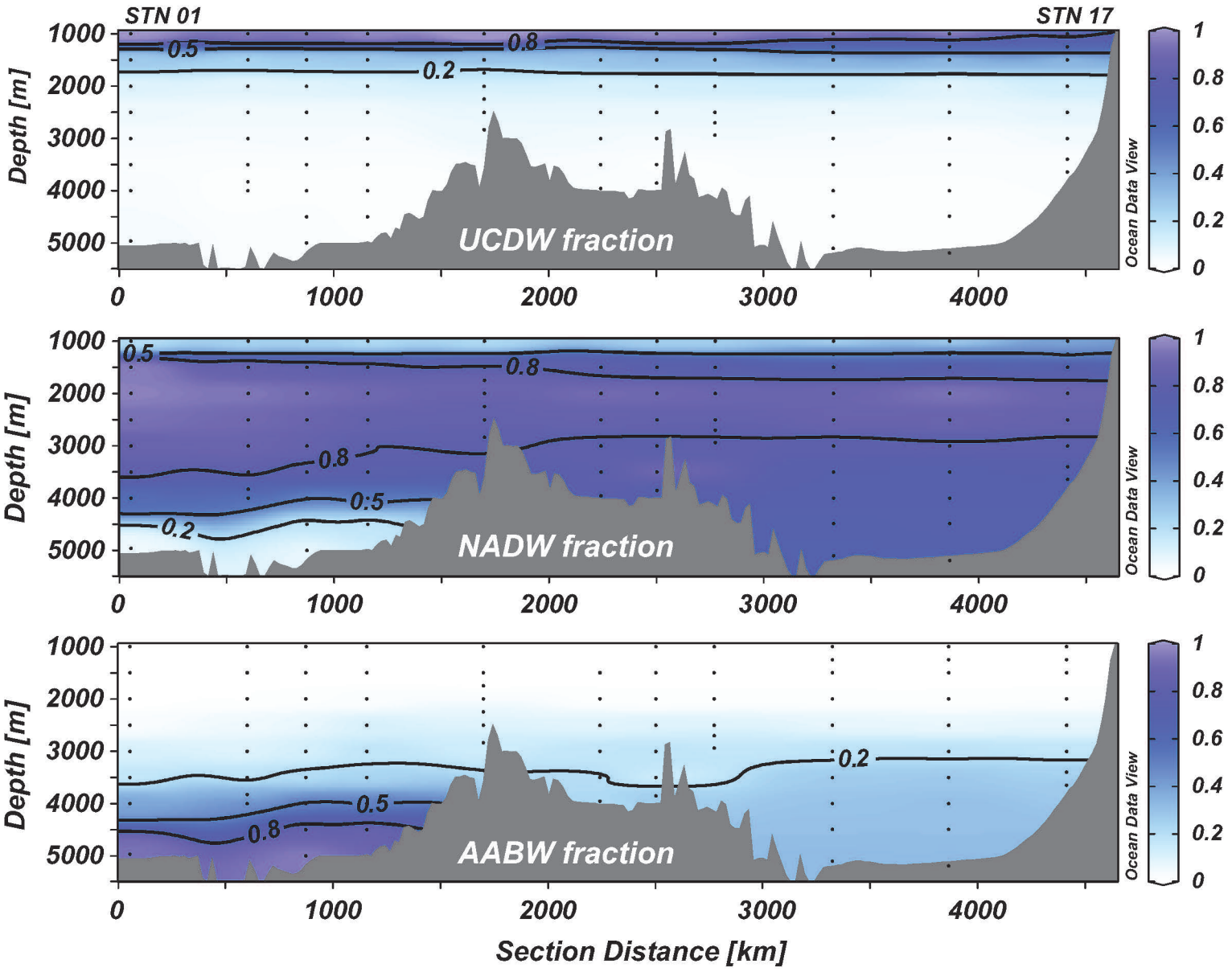

Figure_06_revised

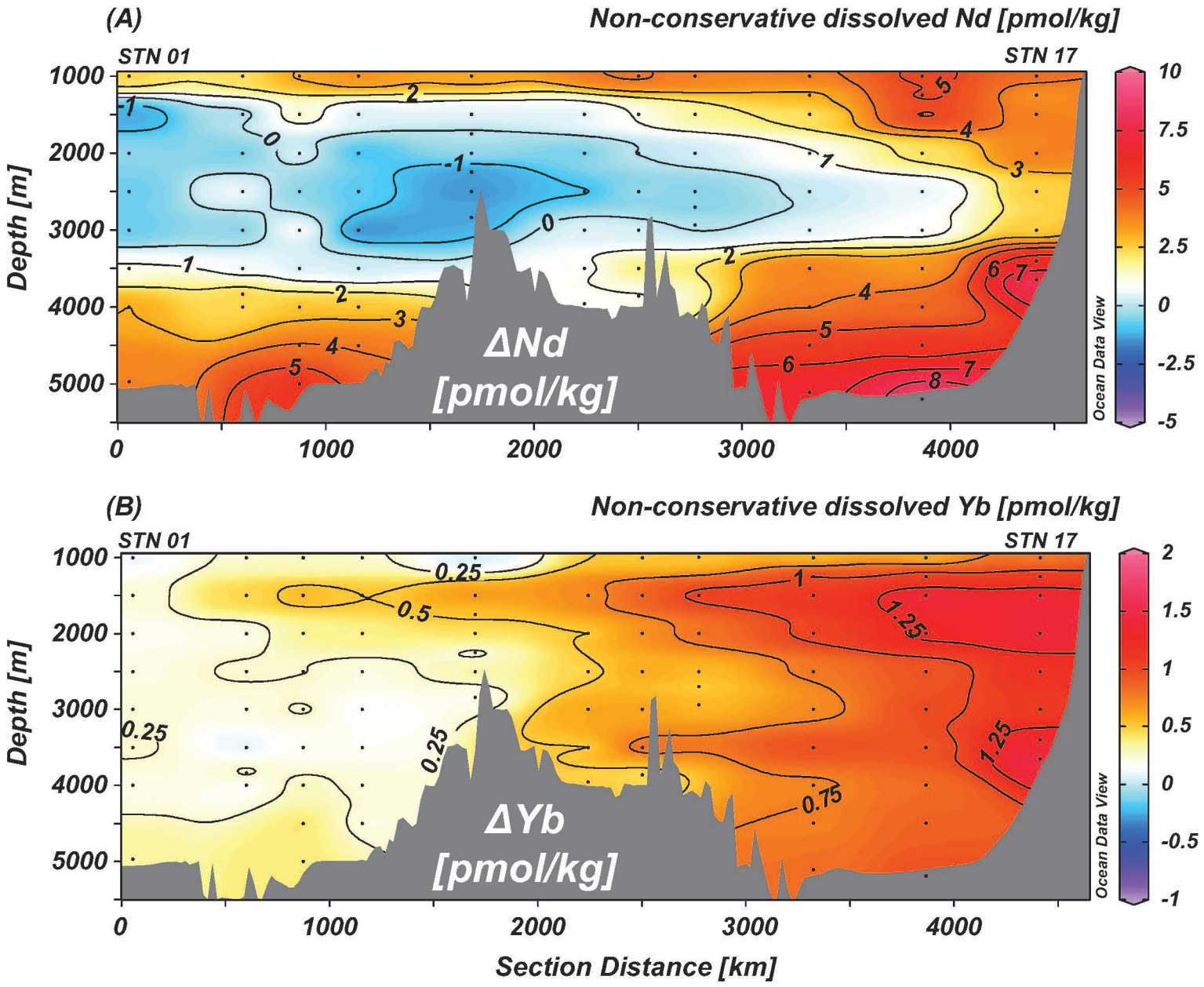

Figure_07_revised

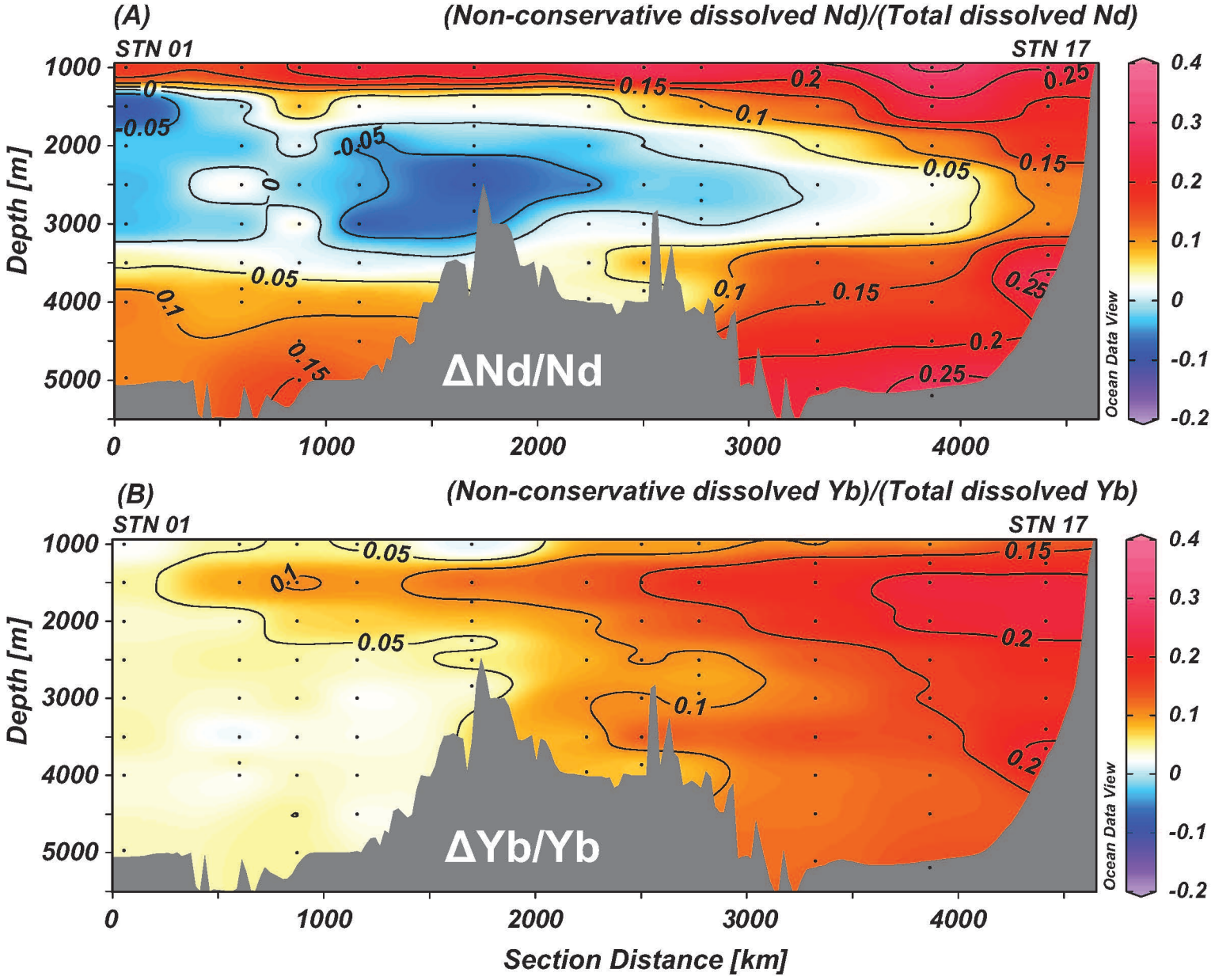

Figure_08_revised

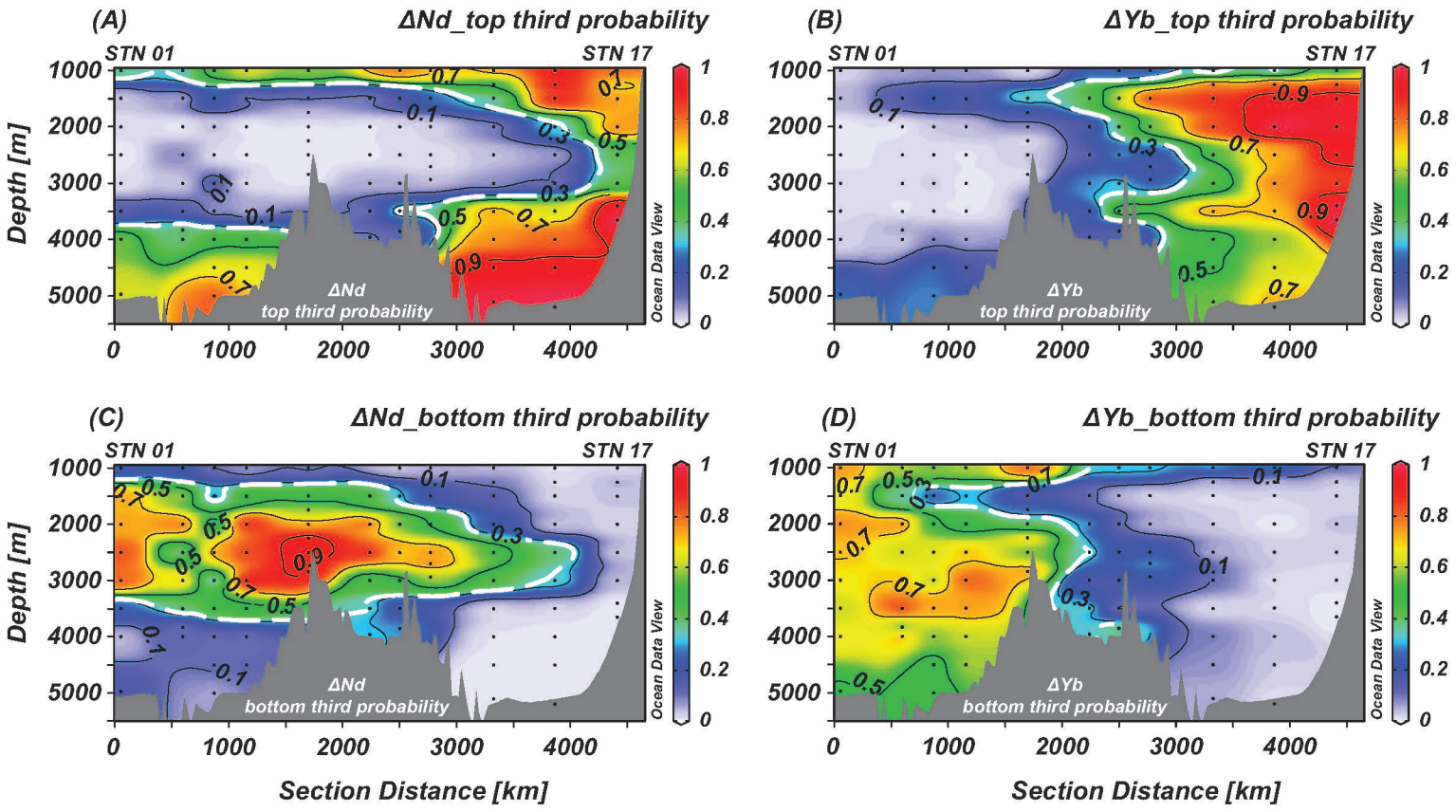

Figure_09

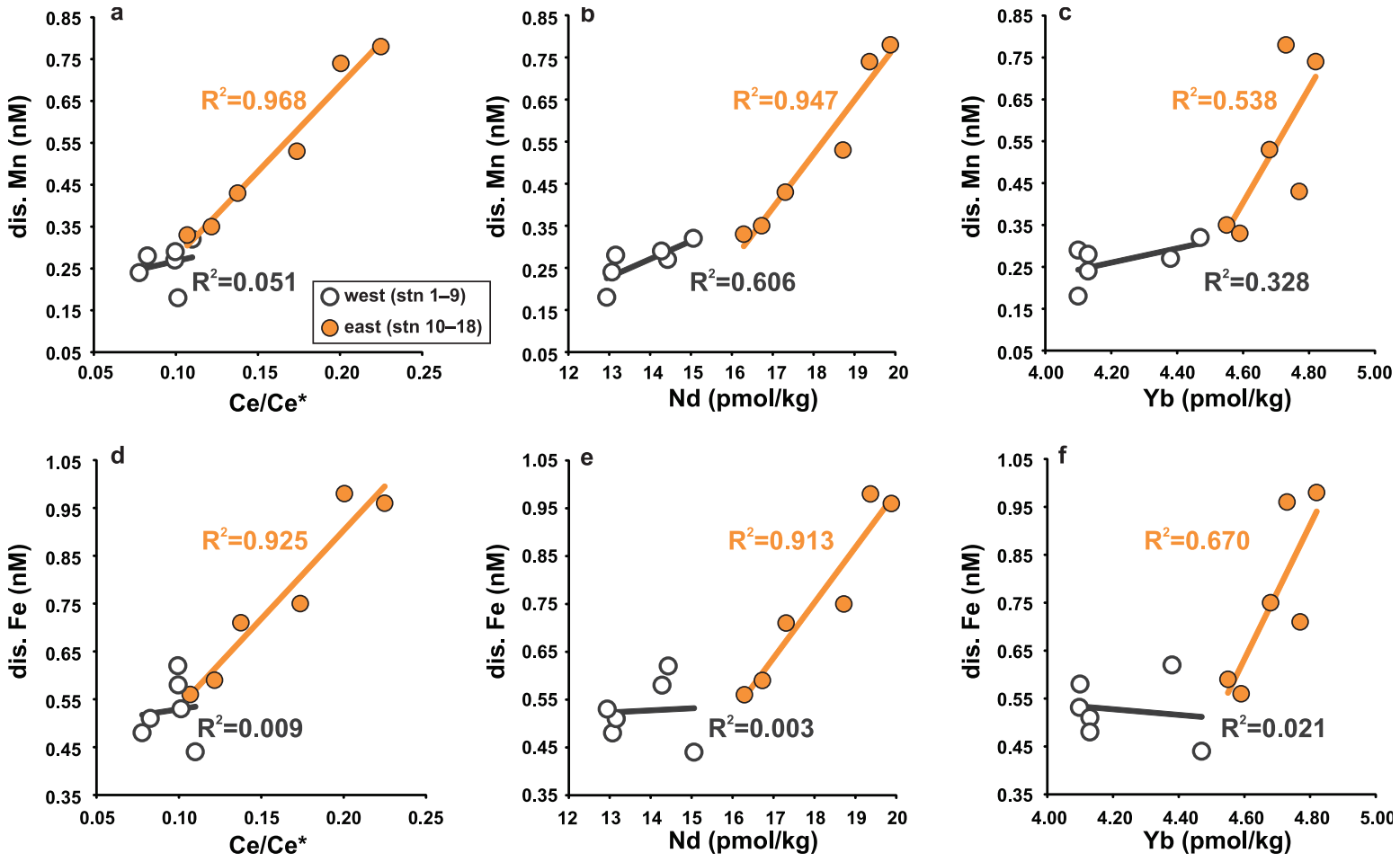
a
b
c
d
e
f
dis. Mn (nM)
dis. Fe (nM)
Ce/Ce*
Nd (pmol/kg)
Yb (pmol/kg)
R²=0.968
R²=0.051
R²=0.947
R²=0.606
R²=0.538
R²=0.328
R²=0.925
R²=0.009
R²=0.913
R²=0.003
R²=0.670
R²=0.021
west (stn 1–9)
east (stn 10–18)

Figure_10_revised

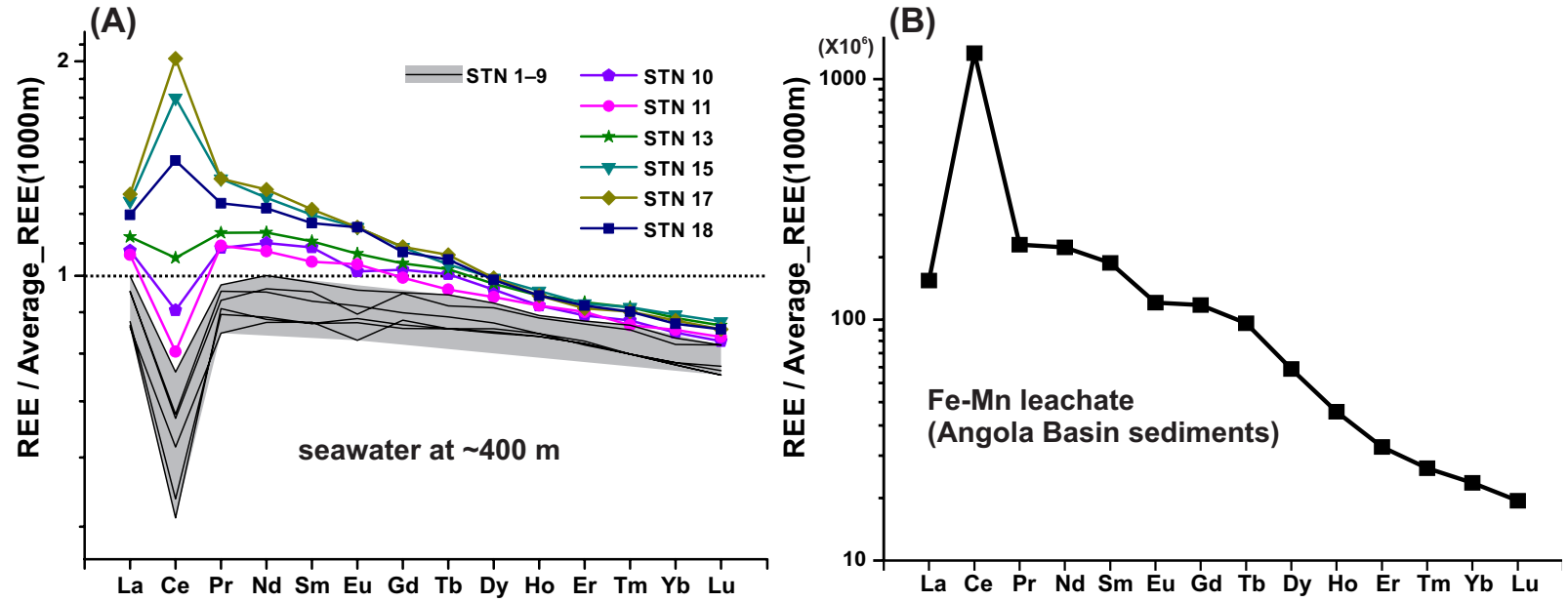

Figure_11

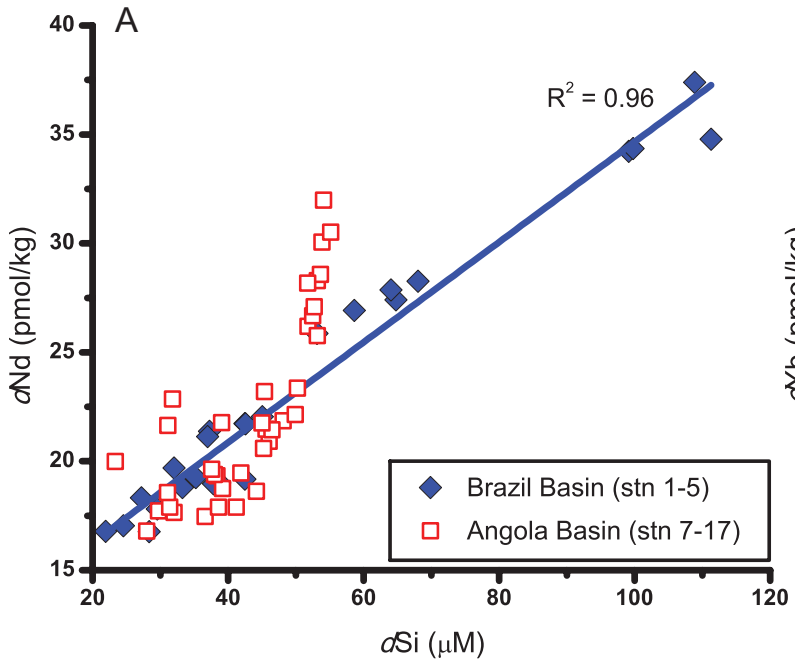
A
R^2 = 0.96
εNd (pmol/kg)
εSi (μM)
Brazil Basin (stn 1-5)
Angola Basin (stn 7-17)

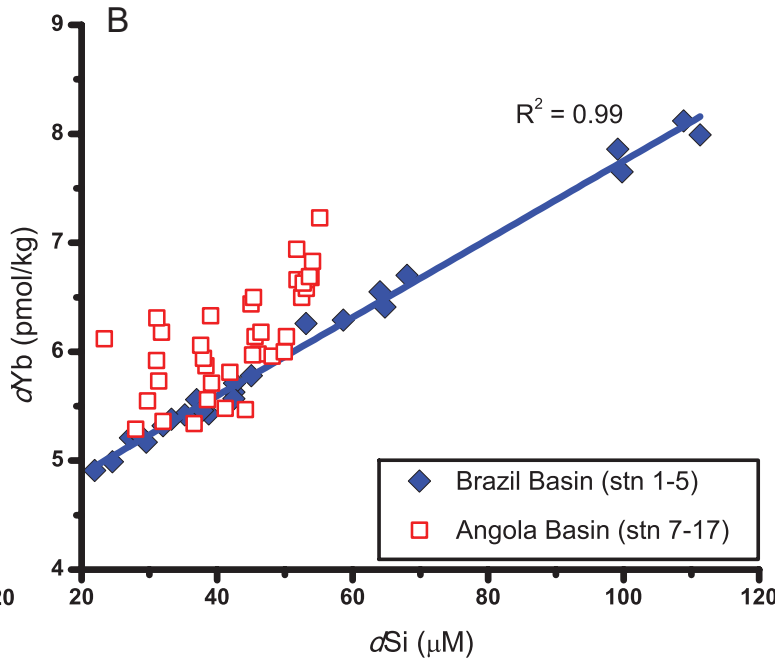
B
R^2 = 0.99
εYb (pmol/kg)
εSi (μM)
Brazil Basin (stn 1-5)
Angola Basin (stn 7-17)

Appendix Table A1 (data table)

Click here to download Appendix: Table A1_CoFeMUG REE.xlsx

Supplemental Material_revised

Click here to download Appendix: CoFeMUG_Supplemental Material_revision.pdf